

# *Ab-initio* predictions of spin relaxation, dephasing and diffusion in solids

Junqing Xu<sup>1,2</sup> and Yuan Ping<sup>3,4,\*</sup>

<sup>1</sup>*Department of Physics, Hefei University of Technology, Hefei, Anhui, China*

<sup>2</sup>*Department of Chemistry and Biochemistry, University of California, Santa Cruz, CA 95064, USA*

<sup>3</sup>*Department of Materials Science and Engineering,  
University of Wisconsin-Madison, WI, 53706, USA*

<sup>4</sup>*Department of Physics, University of California, Santa Cruz, CA, 95064, USA*

(Dated: August 1, 2023)

Spin relaxation, dephasing and diffusion are at the heart of spin-based information technology. Accurate theoretical approaches to simulate spin lifetimes ( $\tau_s$ ), determining how fast the spin polarization and phase information will be lost, are important to the understandings of underlying mechanism of these spin processes, and invaluable to search for promising candidates of spintronic materials. Recently, we develop a first-principles real-time density-matrix (FPDM) approach to simulate spin dynamics for general solid-state systems. Through the complete first-principles' descriptions of light-matter interaction and scattering processes including electron-phonon, electron-impurity and electron-electron scatterings with self-consistent spin-orbit coupling, as well as *ab initio* Landé  $g$ -factor, our method can predict  $\tau_s$  at various conditions as a function of carrier density and temperature, under electric and magnetic fields. By employing this method, we successfully reproduce experimental results of disparate materials and identify the key factors affecting spin relaxation, dephasing, and diffusion in different materials. Specifically, we predict that germanene has long  $\tau_s$  ( $\sim 100$  ns at 50 K), a giant spin lifetime anisotropy and spin-valley locking effect under electric fields, making it advantageous for spin-valleytronic applications. Based on our theoretical derivations and *ab initio* simulations, we propose a new useful electronic quantity, named spin-flip angle  $\theta^{\uparrow\downarrow}$ , for the understanding of spin relaxation through intervalley spin-flip scattering processes. Our method can be further applied to other emerging materials and extended to simulate exciton spin dynamics and steady-state photocurrents due to photogalvanic effect.

## I. INTRODUCTION

In last two decades, spintronics in unconventional semiconductors and metals, including two-dimensional materials and their heterostructures[1, 2], topological and magnetic materials[3, 4], hybrid perovskites[5, 6] etc., have drawn significant interests owing to its unprecedented potentials in microelectronics and next generation low-power electronics. Spin, as a pure quantum mechanical object, is the fundamental information carrier instead of charge, with much less energy dissipation. Ideally one wants such information preserved as long as possible for stable manipulation. Therefore, understanding how spins relax and transport is of central importance in spintronics.

Spin is an unconserved quantity in solids due to its coupling with other quantities, such as electron orbital. Therefore, after excess spins being generated, spin can lose its polarization (relaxation) and phase (dephasing) due to coupling with environment. One critical parameter describing the timescale of such processes is spin lifetime  $\tau_s$  including  $T_1$  (relaxation) and  $T_2$  (dephasing), which is often required to be sufficiently long for stable detection and manipulation of spin. Accurate and reliable theoretical approaches to simulate  $\tau_s$  are demanded for the detailed understandings of spin dynamics and transport phenomena, and designing new spintronics ma-

terials and devices.

Previously, methods based on model Hamiltonian with empirical parameters[1, 7, 8] were extensively employed for simulation of spin relaxation, dephasing, and diffusion in solids. While these methods provide some mechanistic insight, they do not serve as predictive tools for the design of new materials and may sometimes lead to qualitatively incorrect predictions due to the use of simplified electronic structures and interactions.

On the other hand, the existing first-principles methodology for  $\tau_s$  has been mostly based on Fermi's Golden rule[9, 10] considering spin-flip transitions, which is only applicable to systems with inversion symmetry or high spin polarization, not suitable to lots of materials with broken inversion symmetry, promising for quantum computing and spintronics applications [1, 7]. Other first-principles techniques like Time-Dependent Density Functional Theory (TDDFT)[11] are challenging for crystalline systems due to high computational cost for describing phonon relaxations that require large supercells. More importantly, long simulation time over nanoseconds often required by spin relaxation is a major difficulty for TDDFT, which is only practical for tens to a few hundred fs. While spin dynamics based on TDDFT has been recently performed for ultrafast demagnetization of magnetic systems within tens of fs[12–14], the intrinsic time scale and supercell limitations mentioned above remain. A recent development of spin phonon relaxation based on spin-spin correlation function may be a promising pathway, where its applicability for various spin relaxation and dephasing pathways remains to be explored [15].

\* yping3@wisc.edu

To overcome these challenges, we recently developed a first-principles real-time density-matrix (FPDM) approach[16–18] to simulate spin dynamics and pump-probe Kerr-rotation for general solid-state systems. The approach is free from empirical parameters and is thus of great predictive power. Through the complete first-principles descriptions of light-matter interaction and scattering processes including electron-phonon, electron-impurity and electron-electron scatterings with self-consistent spin-orbit coupling (SOC) and Landé  $g$ -factor, our method can predict  $\tau_s$  as a function of temperature and carrier density, under electric and magnetic fields. The method was applied to disparate materials, including semiconductors and metals, with and without inversion symmetry, in good agreement with experimental results[16–21].

In this article, we briefly introduce the theory and implementation of our method, present its applications and show its predictive power using a two-dimensional Dirac material - Germanene as a showcase. Through detailed theoretical analysis, we show how *ab-initio* simulations improve our understandings of spin relaxation mechanisms and are used to identify the key quantities and/or factors to spin relaxation, dephasing, and diffusion. At the end, we discuss how our FPDM approach can be generalized/extended to simulate spin dynamics of excitons, instead of free carriers, and transport properties such as photocurrent and spin currents in broken inversion systems (photogalvanic effect).

## II. THEORY

### A. Density-matrix (DM) master equation

#### 1. Quantum master equation

To provide a general formulation of quantum dynamics in solid-state materials, we start from the Liouville-von Neumann equation in the Schrödinger picture,

$$\frac{d\rho(t)}{dt} = -\frac{i}{\hbar}[H, \rho(t)], \quad (1)$$

$$H = H_0 + H', \quad (2)$$

where  $H$ ,  $H_0$ , and  $H'$  are total, unperturbed and perturbation Hamiltonians respectively. In this work,

$$H_0 = H_e + H_{\text{ph}} + H_{\text{photon}}, \quad (3)$$

$$H' = H_{\text{e-light}} + H_{\text{e-ph}} + H_{\text{e-i}} + H_{\text{e-e}}, \quad (4)$$

where  $H_e$ ,  $H_{\text{ph}}$  and  $H_{\text{photon}}$  are unperturbed single-particle electronic, phonon, and photon Hamiltonian respectively.  $H_{\text{e-light}}$  is the light-matter interaction term.  $H_{\text{e-ph}}$ ,  $H_{\text{e-i}}$  and  $H_{\text{e-e}}$  describe the electron-phonon (e-ph), electron-impurity (e-i), and electron-electron (e-e) interaction, respectively.

In practice, the many-body density matrix in Eq. 1 is reduced to one-particle density matrix for electrons,

where the environmental degree of freedom is traced out[22], with a proper truncated BBGKY hierarchy [23, 24]. The total rate of change of the electronic DM  $\rho$  is separated into terms related to different parts of Hamiltonian,

$$\frac{d\rho}{dt} = \left. \frac{d\rho}{dt} \right|_{\text{coh}} + \left. \frac{d\rho}{dt} \right|_{\text{scatt}}, \quad (5)$$

where  $[H, \rho] = H\rho - \rho H$ .  $\left. \frac{d\rho}{dt} \right|_{\text{coh}}$  describes the coherent dynamics of electrons including the free-particle dynamics, the field-induced dynamics, etc.  $\left. \frac{d\rho}{dt} \right|_{\text{scatt}}$  captures the scattering between electrons and other particles. Their detailed forms are given in the subsections below.

To obtain Eq. 5 which involves only the dynamics of electrons or the electronic subsystem, we have assumed the environmental subsystem is characterized by a huge number of degrees of freedom and is not perturbed by the electronic subsystem; in this work it means there is no dynamics of phonons and photons. Formally this is the prerequisite for the Markovian approximation. This assumption is valid when the system is not far from initial equilibrium, e.g., the excited carrier density is not very high. The inclusion of dynamics of the environment, e.g. phonon degrees of freedom in the dynamics, or formally non-Markovian approximation by taking into account the memory effect of phonon bath, has been discussed in details in Refs. 22, 25.

#### 2. Coherent terms and external fields

In general, a coherent term corresponding to a single-particle electronic Hamiltonian  $H_{\text{sp}}$  reads

$$\left. \frac{d\rho}{dt} \right|_{\text{sp}} = -\frac{i}{\hbar}[H_{\text{sp}}, \rho]. \quad (6)$$

In absence of external fields, the coherent dynamics contains only one term

$$\left. \frac{d\rho}{dt} \right|_{\text{free}} = -\frac{i}{\hbar}[H_e, \rho]. \quad (7)$$

$H_e$  is the unperturbed electronic Hamiltonian, practically computed at the mean-field level, i.e. from density functional theory (DFT). With the electronic eigen-basis,

$$H_{e,kmn} = \epsilon_{kn} \delta_{mn}, \quad (8)$$

where  $k$  is k-point index,  $m$  and  $n$  are band indices,  $\epsilon$  is the single-particle energy, and  $\delta_{mn}$  is Kronecker delta function.

Therefore, we have

$$\left( \left. \frac{d\rho}{dt} \right|_{\text{free}} \right)_{kmn} = -\frac{i}{\hbar} (\epsilon_{km} - \epsilon_{kn}) \rho_{kmn}. \quad (9)$$

We note that the exchange-correlation potential in electronic Hamiltonian could be time-dependent, which

will introduce an additional term in coherent dynamics[8, 26]. We will not discuss in detail here.

The inclusion of external fields in the DM approach for solid-state materials is not trivial and was studied by many theorists since 1950s[27–33]. Here, we consider three spatially homogeneous fields as follows.

*2.1 A laser field.* In this work, we approximate that the light-mater interaction  $H_{e\text{-light}}$  consists of two parts - a semiclassical part  $H_{\text{laser}}$  describing electrons moving in a laser field (i.e., an electromagnetic field caused by the incident laser) and a quantum part describing the electron-photon interaction in the vacuum without considering the laser. The semiclassical part corresponds to light absorption and stimulated emission under a laser field, while the quantum part corresponds to spontaneous emission. We discuss the coherent term due to the semiclassical part first but discuss the quantum part in the next subsection.

The Hamiltonian of a laser with frequency  $\omega_{\text{laser}}$  is approximately[16]

$$H_{\text{laser},kmn}(\omega, t) = \frac{e}{m_e} \mathbf{A}_{\text{laser}}(t) \cdot \mathbf{p}_{kmn} \exp(i\omega_{\text{laser}}t) + H.C., \quad (10)$$

where  $H.C.$  is Hermitian conjugate.  $\mathbf{A}_{\text{laser}}(t)$  is the amplitude.  $\mathbf{A}_{\text{laser}}(t)$  is real (complex) for linearly (circularly) polarized light.  $\mathbf{p}_{kmn}$  is the momentum operator matrix element. Note that to include the contribution from the nonlocal part of the pseudopotentials, momentum operator is computed with commutator  $[\mathbf{r}, H_e] = \nabla$ .

For a Gaussian pump pulse centered at time  $t_{\text{center}}$  with width  $\tau_{\text{pump}}$ ,

$$\mathbf{A}_{\text{laser}}(t) = \mathbf{A}_{\text{laser}} \frac{1}{\sqrt{\sqrt{\pi}\tau_{\text{pump}}}} \exp\left[-\frac{(t-t_{\text{center}})^2}{2\tau_{\text{pump}}^2}\right]. \quad (11)$$

Note that the corresponding pump power is  $I_{\text{laser}} = \omega_{\text{laser}}^2 |\mathbf{A}_{\text{laser}}|^2 / (8\pi\alpha)$ , where  $\alpha$  is fine structure constant.

The corresponding dynamics is

$$\frac{d\rho}{dt}|_{\text{laser}} = -\frac{i}{\hbar} [H_{\text{laser}}, \rho]. \quad (12)$$

*2.2 A static electric field along a non-periodic direction.* Such electric field along non-periodic direction  $E_{\text{np}}$  is directly included in the DFT calculation and is modeled by a ramp or saw-like potential. Under such treatment,  $H_e$  is  $E_{\text{np}}$ -dependent. As all terms of the master equation (Eq. 5) are built on eigensystems from  $H_e$ , they are all  $E_{\text{np}}$ -dependent. However, if electric field is applied along the periodic direction, one needs to properly treat the periodic boundary condition (e.g. using the modern theory of polarization [34, 35]).

*2.3 A magnetic field.* We describe the effects of an external magnetic field  $\mathbf{B}^{\text{ext}}$  using Zeeman Hamiltonian

$$H_{Z,k}(\mathbf{B}^{\text{ext}}) = \mu_B \mathbf{B}^{\text{ext}} \cdot (\mathbf{L}_k + g_0 \mathbf{S}_k), \quad (13)$$

where  $\mu_B$  is Bohr magneton;  $g_0$  is the free-electron  $g$ -factor;  $\mathbf{S}$  and  $\mathbf{L}$  are the spin and orbital angular momentum respectively. The simulation of  $\mathbf{L}$  is nontrivial for periodic systems. With the Blöch basis, the orbital angular momentum reads

$$\mathbf{L}_{k,mn} = i \left\langle \frac{\partial u_{km}}{\partial \mathbf{k}} \right| \times \left( \hat{H}_e(\mathbf{B}^{\text{ext}} = 0) - \bar{\epsilon}_{kmn} \right) \left| \frac{\partial u_{kn}}{\partial \mathbf{k}} \right\rangle, \quad (14)$$

$$\bar{\epsilon}_{kmn} = \frac{\epsilon_{km} + \epsilon_{kn}}{2}, \quad (15)$$

where  $u$  is the periodic part of the single-particle wavefunction;  $\hat{H}_e(\mathbf{B}^{\text{ext}} = 0)$  is the zero-field Hamiltonian operator. Eqs. 14 - 15 can be proven equivalent to  $\mathbf{L} = \mathbf{0.5} * (\mathbf{r} \times \mathbf{p} - \mathbf{p} \times \mathbf{r})$  with  $\mathbf{r}$  the position operator. The detailed implementation of Eq. 14 is described in Ref. 36.

There are two ways to consider magnetic-field effects. The first way is including  $H_{Z,k}(\mathbf{B}^{\text{ext}})$  in  $H_e$  perturbatively (instead of self-consistently), then the new eigensystems can be obtained by diagonalizing  $H_e(\mathbf{B}^{\text{ext}} \neq 0)$ . The second way is including  $H_{Z,k}(\mathbf{B}^{\text{ext}})$  in  $H'$  and the corresponding coherent dynamics is  $-\frac{i}{\hbar} [H_{Z,k}(\mathbf{B}^{\text{ext}}), \rho]$ . In practice, the two approaches lead to nearly the same dynamical quantities such as lifetimes, since  $H_{Z,k}(\mathbf{B}^{\text{ext}})$  is rather weak - e.g. Zeeman splitting under 1 Tesla is of order 0.1 meV for many solid-state systems. In addition, we note that we do not consider the effect of very strong magnetic field such as the appearance of Landau level in this work.

### 3. Scattering terms

The scattering part of quantum master equation can be separated into contributions from several scattering channels,

$$\frac{d\rho}{dt}|_{\text{scatt}} = \sum_c \frac{d\rho}{dt}|_c, \quad (16)$$

where  $c$  labels a scattering channel corresponding to an interaction Hamiltonian  $H_c$ . Under Born-Markov approximation and neglecting renormalization of single particle energies, in general we have[37]

$$\frac{d\rho_{12}}{dt}|_c = \frac{1}{2} \sum_{345} \begin{bmatrix} (I - \rho)_{13} P_{32,45}^c \rho_{45} \\ -(I - \rho)_{45} P_{45,13}^{c,*} \rho_{32} \end{bmatrix} + H.C., \quad (17)$$

where  $P^c$  is the generalized scattering matrix and  $H.C.$  denotes Hermitian conjugate. The subindex, e.g., “1”, is the combined index of  $\mathbf{k}$ -point and band. The weights of  $\mathbf{k}$  points must be considered when summing over  $\mathbf{k}$  points.

*3.1 Electron-phonon.* The electron-phonon (e-ph) scattering matrix is given by[37]

$$P_{1234}^{e-ph} = \sum_{q\lambda\pm} A_{13}^{q\lambda\pm} A_{24}^{q\lambda\pm,*}, \quad (18)$$

$$A_{13}^{q\lambda\pm} = \sqrt{\frac{2\pi}{\hbar}} g_{13}^{q\lambda\pm} \sqrt{\delta_{\sigma}^G(\omega_{13} \pm \omega_{q\lambda})} \sqrt{n_{q\lambda}^{\pm}}, \quad (19)$$

$$\omega_{13} = \epsilon_1 - \epsilon_3, \quad (20)$$

where  $q$  and  $\lambda$  are phonon wavevector and mode,  $g^{q\lambda\pm}$  is the e-ph matrix element, resulting from the absorption (-) or emission (+) of a phonon,  $n_{q\lambda}^{\pm} = n_{q\lambda} + 0.5 \pm 0.5$  in terms of phonon Bose factors  $n_{q\lambda}$ , and  $\delta_{\sigma}^G$  represents an energy conserving  $\delta$ -function broadened to a Gaussian of width  $\sigma$ . The explicit derivation of Lindbladian dynamics and scattering matrix can be found in Ref. [37]. This form guarantees the positive definition of density matrix.  $g^{q\lambda\pm}$  is computed fully from first-principles with self-consistent spin-orbit coupling based on density-functional perturbation theory and Wannier interpolation methods[38].

*3.2 Electron-impurity.* Similar to the e-ph scattering, we write electron-impurity scattering as

$$P_{1234}^{e-i} = A_{13}^i A_{24}^{i,*}, \quad (21)$$

$$A_{13}^i = \sqrt{\frac{2\pi}{\hbar}} g_{13}^i \sqrt{\delta_{\sigma}^G(\omega_{13})} \sqrt{n_i V_{\text{cell}}}, \quad (22)$$

$$g_{13}^i = \langle 1 | \Delta V^i | 3 \rangle, \quad (23)$$

$$\Delta V^i = V^i - V^0, \quad (24)$$

where  $n_i$  and  $V_{\text{cell}}$  are impurity density and unit cell volume, respectively,  $V^i$  is the potential of the impurity system and  $V^0$  is the potential of the pristine system. Here we assume impurities are randomly distributed and impurity density is sufficiently low so that the average distance between neighboring impurities is sufficiently long with nearly no interactions among impurities.

In this work,  $g^i$  of neutral and ionized impurities are computed differently as follows.

For neutral impurities,  $V^i$  is computed with SOC using a large supercell including an impurity. To speed up the supercell convergence, we used the potential alignment method developed in Ref. 39.

For ionized impurities, we approximate  $\Delta V^i$  as the potential of point charge and is simply the product of the impurity charge  $Z$  and the screened Coulomb potential[40]. Such approximate  $\Delta V^i$  is accurate in the long-range limit,[40] i.e., its Fourier transform  $\Delta V^i(q)$  is accurate when  $q \rightarrow 0$ , so that it is most suitable for intravalley relaxation process due to electron-impurity scatterings. The justification of this approximation is that the long-range part is the most dominant in the electrostatic interaction of ionized impurities[40].

*3.3 Electron-electron interaction.* The e-e scattering matrix is given by[37]

$$P_{1234}^{e-e} = 2 \sum_{56,78} (I - \rho)_{65} \mathcal{A}_{15,37} \mathcal{A}_{26,48}^* \rho_{78}, \quad (25)$$

$$\mathcal{A}_{1234} = \frac{1}{2} (A_{1234} - A_{1243}), \quad (26)$$

$$A_{1234} = \frac{1}{2} \sqrt{\frac{2\pi}{\hbar}} \left[ g_{1234}^{e-e} (\delta_{\sigma}^G(\omega_{1234}))^{1/2} + g_{2143}^{e-e} (\delta_{\sigma}^G(\omega_{2143}))^{1/2} \right], \quad (27)$$

$$g_{1234}^{e-e} = \langle 1(r) | \langle 2(r') | V(r-r') | 3(r) | 4(r') \rangle, \quad (28)$$

where  $V(r-r')$  is the screened Coulomb potential and  $\delta_{\sigma}^G(\omega_{1234}) = \delta_{\sigma}^G(\epsilon_1 + \epsilon_2 - \epsilon_3 - \epsilon_4)$  is a Gaussian-broadened energy conservation function. The screening is described by Random-Phase-Approximation (RPA) dielectric function. We note that unlike the e-ph and e-i channels,  $P^{e-e}$  is a function of  $\rho$  and needs to be updated during time evolution of  $\rho$ . This is a clear consequence of the two-particle nature of e-e scattering.  $P^{e-e}$  can be written as the difference between a direct term ( $P^{e-e,d}$ ) and an exchange term ( $P^{e-e,x}$ ),

$$P^{e-e} = P^{e-e,d} - P^{e-e,x}, \quad (29)$$

$$P^{e-e,d} = \sum_{56,78} (I - \rho)_{65} A_{15,37} A_{26,48}^* \rho_{78}, \quad (30)$$

$$P^{e-e,x} = \sum_{56,78} (I - \rho)_{65} A_{15,37} A_{26,84}^* \rho_{78}. \quad (31)$$

According to Ref. 22, the direct term is expected to dominate the dynamical scattering processes among conduction electrons or valence electrons, allowing us to neglect the exchange term here.

Currently, we use the static Random Phase Approximation (RPA) dielectric function for the screening without local-field effects. Given the intraband transition is more important, we take the approximate dielectric function as:

$$\epsilon(\mathbf{q}) = \epsilon_s \epsilon^{\text{intra}}(\mathbf{q}), \quad (32)$$

where  $\epsilon_s$  is the static dielectric constant well-defined for insulators, calculated by Density Functional Perturbation Theory (DFPT)[41].  $\epsilon_s$  effectively takes into account the interband contribution in the dielectric screening.  $\epsilon^{\text{intra}}(\mathbf{q})$  is the intraband contribution which involves only states with free carriers and is critical for doped semiconductors (with free carriers). We computed it at RPA without local field effect,

$$\epsilon^{\text{intra}}(\mathbf{q}) = 1 - V^{\text{bare}}(\mathbf{q}) \sum_{\mathbf{k}mn} \left( \frac{f_{\mathbf{k}-\mathbf{q},m} - f_{\mathbf{k}n}}{\epsilon_{\mathbf{k}-\mathbf{q},m} - \epsilon_{\mathbf{k}n}} \times \frac{1}{|\langle u_{\mathbf{k}-\mathbf{q},m} | u_{\mathbf{k}n} \rangle|^2} \right), \quad (33)$$

where the sum runs over only states having free carriers, e.g., for a n-doped semiconductor,  $m$  and  $n$  are conduction band indices. In the formula above,  $f$  is

time-dependent non-equilibrium occupation instead of the equilibrium one  $f^{\text{eq}}$ . Therefore, if the optical field  $\mathbf{A}_{\text{laser}}(t)$  is activated,  $\varepsilon^{\text{intra}}(\mathbf{q})$  will be updated in every time step, as  $f$  will differ from  $f^{\text{eq}}$  and the difference depends on the excitation density.  $V^{\text{bare}}(\mathbf{q}) = e^2 / (V_{\text{cell}} \varepsilon_0 |q|^2)$  is the bare Coulomb potential with  $\varepsilon_0$  vacuum permittivity.

We then have the matrix elements in reciprocal space,

$$g_{1234}^{\text{e-e}} = V^{\text{scr}}(\mathbf{q}_{13}) \delta_{\mathbf{k}_1 + \mathbf{k}_2, \mathbf{k}_3 + \mathbf{k}_4} \langle u_1 | u_3 \rangle \langle u_2 | u_4 \rangle, \quad (34)$$

$$V^{\text{scr}}(\mathbf{q}_{13}) = V^{\text{bare}}(\mathbf{q}_{13}) / \varepsilon(\mathbf{q}_{13}), \quad (35)$$

where  $V^{\text{scr}}(\mathbf{q})$  is the screened Coulomb potential and  $\mathbf{q}_{13} = \mathbf{k}_1 - \mathbf{k}_3$ .  $\langle u_1 | u_3 \rangle$  is the overlap matrix element between two periodic parts of Bloch wave functions.

(iv) *Spontaneous emission.* As discussed above, in this work, the light-matter interaction consists of a semiclassical part (absorption and simulated emission by a laser field) and a quantum part. The semiclassical part has been discussed above (Sec. II A 2). Here we discuss the quantum part, which describes the electron-photon interaction in the vacuum. Similar to the electron-phonon scattering, we write a similar form for electron-photon interaction (the underlying consideration on positive definition of density matrix is similar) [37].

$$P_{1234}^{\text{sp-em}} = \sum_{q\lambda\pm} A_{13}^{\text{photon},q\lambda\pm} A_{24}^{\text{photon},q\lambda\pm,*}, \quad (36)$$

$$A_{13}^{\text{photon},q\lambda\pm} = \sqrt{\frac{2\pi}{\hbar}} g_{13}^{\text{photon},q\lambda\pm} \sqrt{\delta_{\sigma}^G(\omega_{13} \pm \omega_{q\lambda}^{\text{photon}})} \quad (37)$$

$$\times \sqrt{n_{q\lambda}^{\text{photon},\pm}}, \quad (38)$$

where “+” and “-” correspond to photon emission and absorption respectively,  $\lambda$  is the photon mode,  $g_{13}^{\text{photon},q\lambda\pm}$  is the electron-photon matrix element proportional to  $\mathbf{p}$  matrix element. The differences from  $P^{\text{e-ph}}$  are: (i) As  $\omega^{\text{photon}}$  is comparable to the band gap which is much greater than  $k_B T$ ,  $n_{q\lambda}^{\text{photon},-} \approx 0$  and  $n_{q\lambda}^{\text{photon},+} \approx 1$ . This represents that photon absorption is not allowed in vacuum, and every photon emission process emits one photon. (ii) As photon momentum  $q$  is tiny (at long wavelength limit), for  $A_{13}^{\text{photon}}$ , we have  $\mathbf{k}_1 \approx \mathbf{k}_3$ . Therefore,

$$A_{13}^{\text{photon},q\lambda+} = \sqrt{\frac{2\pi}{\hbar}} g_{13}^{\text{photon},q\lambda+} \sqrt{\delta_{\sigma}^G(\omega_{13} + \omega_{q\lambda}^{\text{photon}})} \delta_{\mathbf{k}_1 \mathbf{k}_3}. \quad (39)$$

The detailed form of  $P_{1234}^{\text{sp-em}}$  will be given in our future work.

## B. Spin lifetime and spin diffusion length

### 1. Spin lifetime: relaxation and dephasing

In most spin lifetime  $\tau_s$  experiments,  $\tau_s$  of ensemble spins are measured. The spin observable of an ensemble is

$$S_i^{\text{tot}}(t) = \text{Tr}[s_i \rho(t)] = \sum_k \sum_{mn} s_{i,kmn} \rho_{knm}(t), \quad (40)$$

where  $s_i$  is spin Pauli matrix in Bloch basis along direction  $i$ . For spin dynamics, the total excited or excess spin observable is often more relevant and is defined as,

$$S_i^{\text{ex}}(t) = S_i^{\text{tot}}(t) - S_i^{\text{eq}}(t), \quad (41)$$

where “eq” corresponds to the final equilibrium state.

The time evolution must start at an initial state (at  $t = t_0$ ) with a net spin i.e.  $\delta\rho(t_0) = \rho(t_0) - \rho^{\text{eq}} \neq 0$  such that  $S_i^{\text{ex}}(t) \neq 0$ . We evolve  $\rho(t)$  through the quantum master equation Eq. 5 for a long enough simulation time, typically from a few ps to a few hundred ns, until the evolution of  $S_i^{\text{ex}}(t)$  can be reliably fitted by

$$S_i^{\text{ex}}(t) = S_i^{\text{ex}}(t_0) \exp\left[-\frac{t-t_0}{\tau_{s,i}}\right] \times \cos[\omega(t-t_0) + \phi] \quad (42)$$

to extract the relaxation time,  $\tau_{s,i}$ . Above,  $\omega$  is oscillation frequency due to Larmor precession.

In Ref. 16, we have shown that one can generate the initial spin imbalance by applying a test magnetic field at  $t = -\infty$ , allowing the system to equilibrate with a net spin and then turning it off suddenly at  $t_0$ , in order to measure spin relaxation.

Historically, spin relaxation time (or longitudinal time)  $T_1$  and ensemble spin dephasing time (or transverse time)  $T_2^*$  were used to characterize the decay of spin ensemble [8, 42]. Suppose the spins of the system are polarized along direction  $\mathbf{r}_0$ , possibly due to applying a constant external field  $\mathbf{B}_0$  along  $\mathbf{r}_0$ , and suppose the total excess/excited spin is along direction  $\mathbf{r}_1$ , if  $\mathbf{r}_1 \parallel \mathbf{r}_0$  (or  $\mathbf{r}_1 \perp \mathbf{r}_0$ ),  $\tau_s$  is called  $T_1$  (or  $T_2^*$ ). For  $T_2^*$ , the excess spin  $\mathbf{S}^{\text{ex}}(t)$  precesses with a frequency proportional to  $|\mathbf{B}_0|$ .

The ensemble spin dephasing rate  $1/T_2^*$  consists of reversible part and irreversible part. The reversible part may be removed by the spin echo technique. The irreversible part is called spin dephasing rate  $1/T_2$ , which must be smaller than  $1/T_2^*$ . According to Ref. 42,  $T_2$  may be also defined using Eq. 43 without the need of spin echo but instead of  $S_i^{\text{tot}}(t)$ , we need another quantity - the sum of individual spin amplitudes

$$S_i^{\text{indiv}} = \sum_k \sum_{mn} |s_{i,kmn} \rho_{knm}(t)|. \quad (43)$$

## 2. Optical measurements

Experimentally,  $\tau_s$  is often studied through ultra-fast magneto-optical pump-probe measurements[43, 44] where excess spin is generated by a circularly-polarized pump pulse and its evolution is detected by probe pulses.

The probe pulse interacts with the material similarly to the pump pulse, and could be described in exactly the same way in principle. However, this would require repeating the simulation for several values of the pump-probe delay. Instead, since the probe is typically chosen to be of sufficiently low intensity, we use second-order time-dependent perturbation theory to capture its interaction with the system [16],

$$\Delta\rho^{\text{probe}} = \frac{1}{2} \sum_{345} \left\{ \begin{array}{l} [I - \rho(t)]_{13} P_{32,45}^{\text{probe}} \rho(t)_{45} \\ - [I - \rho(t)]_{45} P_{45,13}^{\text{probe}} \rho(t)_{32} \end{array} \right\} + H.C., \quad (44)$$

$$P_{1234}^{\text{probe}} = \sum_{\pm} A_{13}^{\text{probe},\pm} A_{24}^{\text{probe},\pm,*}, \quad (45)$$

$$A_{13}^{\text{probe},\pm} = \sqrt{\frac{2\pi}{\hbar}} \frac{e}{m_e} (\mathbf{A}^{\text{probe}} \cdot \mathbf{p}) \sqrt{\delta_{\sigma}^G(\omega_{13} \pm \omega^{\text{probe}})} \quad (46)$$

The change of dielectric function  $\Delta\epsilon$  between the excited state and ground state absorption detected by the probe is then

$$\text{Im}\Delta\epsilon = \frac{2\pi}{(\omega^{\text{probe}})^3 |\mathbf{A}^{\text{probe}}|^2} \text{Tr}(H_0 \Delta\rho^{\text{probe}}). \quad (47)$$

Note that  $\Delta\rho^{\text{probe}}$  contains  $|\mathbf{A}^{\text{probe}}|^2$  so that  $\text{Im}\Delta\epsilon$  is independent of  $\mathbf{A}^{\text{probe}}$ . The  $\text{Im}\Delta\epsilon$  above is a functional of  $\rho$  according to Eq. 44 and is an extension of the usual independent-particle  $\text{Im}\epsilon$  depending on just occupation function  $f$ [45]. After obtaining  $\text{Im}\Delta\epsilon$ , the real part  $\text{Re}\Delta\epsilon$  can be obtained from the Kramers-Kronig relation.

By summing up  $\Delta\epsilon$  with the dielectric function for ground state absorption, we can obtain the excited-state  $\epsilon$  as inputs for Kerr and Faraday rotation calculations[46]. These correspond to the rotations of the polarization plane of a linearly-polarized light, reflected by (Kerr rotation) and transmitted (Faraday rotation) through the material, after a pump excitation with a circularly-polarized light. Time-Resolved Kerr/Faraday Rotation (TRKR/TRFR) has been widely used to study spin dynamics of solids[47, 48]. In a TRKR experiment, a circularly-polarized pump pulse is used to excite valence electrons to conduction bands. The transitions approximately satisfy the selection rule of  $\Delta m_j = \pm 1$  for left and right circularly-polarized pulses, respectively, where  $m_j$  is secondary total angular momentum. TRKR works by measuring the polarization changes of reflected light, which qualitatively is proportional to the small population imbalance of electronic states with different  $m_j$ .

Specifically, the Kerr rotation angle  $\theta_K$  is computed with dielectric functions by

$$\theta_K = \text{Im} \frac{\sqrt{\epsilon_+} - \sqrt{\epsilon_-}}{1 - \sqrt{\epsilon_+} \sqrt{\epsilon_-}}, \quad (48)$$

where  $\pm$  denotes the left and right circular polarization, respectively.

## 3. The work flow of a spin dynamics simulation

As shown in Fig. 1, a spin dynamics simulation has three main steps:

(i) **DFT step.** The ground-state electronic structure, phonons, as well as the e-ph and e-i matrix elements are firstly calculated using density functional theory (DFT) with relatively coarse  $k$  and  $q$  meshes in the DFT plane-wave code JDFTx[49]. The phonon calculation uses the finite difference method with supercells. Alternatively, we can compute the same quantities in QuantumEspresso, with phonon and e-ph couplings calculated by DFPT at the coarse mesh as well.

(ii) **Wannier step.** We then transform all quantities from plane wave basis to maximally localized Wannier function basis[50], and interpolate them[38, 51–55] to substantially finer  $k$  and  $q$  meshes. The Wannier interpolation approach fully accounts for long-range polar terms (originally from LO-TO splitting) in the e-ph matrix elements and phonon dispersion relations using the approaches of Ref. 56 and 57 for the 3D and 2D systems. This part is performed in JDFTx code.

(iii) **Dynamics step.** Starting from an initial state with a spin imbalance, we evolve  $\rho(t)$  through the quantum master equation of Eq. 5. After obtaining spin observable  $S(t)$  from  $\rho(t)$  (Eq. 40) and fitting  $S(t)$  to an exponentially oscillating decay curve (Eq. 43), the decay constant  $\tau_s$  is obtained. This part is performed in the DMD code interfacing with the JDFTx code.

## 4. Carrier lifetime and spin diffusion length

**4.1 Semiclassical limit and carrier lifetime.** At the semiclassical limit,  $\rho$  is replaced by (non-equilibrium) occupation  $f$ , then the scattering term originally with a full quantum description in Eq. 17 required by DM dynamics becomes [16]:

$$\frac{df_1}{dt}|_c = \sum_{2 \neq 1} [(1 - f_1) P_{11,22}^c f_2 - (1 - f_2) P_{22,11}^c f_1], \quad (49)$$

using the facts that  $P_{11,22}$  is real and “2=1” term is zero. “c” represent a scattering channel. Note that the weights of  $k$  points must be considered when summing over  $k$  points.

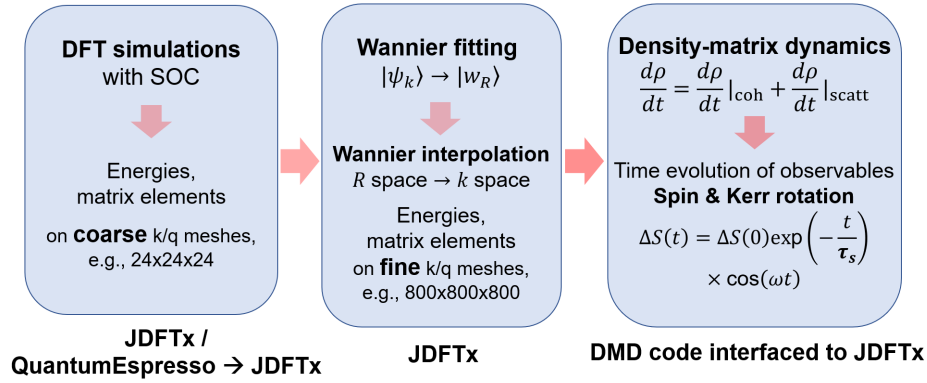


FIG. 1. The work flow of a spin dynamics simulation. The codes implemented for different steps are listed and explained in the main text.

Suppose  $f$  is perturbed from its equilibrium value by  $\delta f$ , i.e.,  $f = f^{\text{eq}} + \delta f$ , then insert  $f$  after perturbation into Eq. 49 and linearize it,

$$\frac{df_1}{dt}|_c = - \sum_{2 \neq 1} [P_{11,22}^c f_2^{\text{eq}} + (1 - f_2^{\text{eq}}) P_{22,11}^c] \delta f_1, \quad (50)$$

using the fact that  $\delta P_{11,22}$  is always zero, even for the e-e scattering.

Define carrier/particle lifetime of state “1”  $\tau_{p,1}^c$  by  $\frac{df_1}{dt}|_c = -\frac{\delta f_1}{\tau_{p,1}^c}$ , we have

$$\frac{1}{\tau_{p,1}^c} = \sum_{2 \neq 1} [P_{11,22}^c f_2^{\text{eq}} + (1 - f_2^{\text{eq}}) P_{22,11}^c]. \quad (51)$$

The linewidth or the imaginary part of self-energy for the scattering channel  $c$  is related to  $\tau_p^c$  by  $\text{Im}\Sigma_1^c = \hbar / (2\tau_{p,1}^c)$ .

**4.2 Spin diffusion length.** The DM approach has been widely employed to simulate transport properties[27, 58, 59] including spin diffusion length  $l_s$ .[8] The implementation of simulating  $l_s$  based on FPDM approach for general solid-state materials is however still under development.

In this work,  $l_s$  are obtained from first-principles using the commonly-used relation[7, 8] based on the drift-diffusion model,

$$l_s = \sqrt{D\tau_s}, \quad (52)$$

$$D = -\mu_c n_c / \frac{dn_c}{d\varepsilon_{\mu_F}}, \quad (53)$$

where  $D$  is the diffusion coefficient of carriers calculated using the generalized Einstein relation[60]. The underlying assumption here is the diffusion coefficient of carrier being the same as spin, which was shown to be true in graphene-derived systems experimentally[61].  $\varepsilon_{\mu_F}$  is the electron chemical potential.  $n_c$  is the carrier density.  $\mu_c$  is the carrier mobility calculated by solving the

linearized Boltzmann equation in momentum-relaxation-time approximation[62–64],

$$\mu_{c,i} = \frac{e}{n_c V_u N_k} \sum_1 [f^{\text{eq}}]_1' v_{1,i}^2 \tau_{m,1}, \quad (54)$$

where  $i = x, y, z$ .  $N_k$  is the number of  $k$  points.  $V_u$  is the unit cell volume.  $n_c$  is electron density.  $[f^{\text{eq}}]'$  is the derivative of the Fermi-Dirac distribution function.  $v$  is the band velocity.  $\tau_m$  is the momentum relaxation time and is approximated as[62–64]

$$\tau_{m,1}^{-1} = \sum_{2 \neq 1} \{ [P_{11,22} f_2^{\text{eq}} + (1 - f_2^{\text{eq}}) P_{22,11}] \cos\theta_{12} \}, \quad (55)$$

$$\cos\theta_{12} = \frac{\mathbf{v}_1 \cdot \mathbf{v}_2}{v_1 v_2}, \quad (56)$$

where  $\mathbf{v}$  is the velocity vector. We find that  $\tau_m$  is similar to the carrier lifetime  $\tau_p$  except the angle factor  $\cos\theta_{12}$ .

### III. SPIN RELAXATION MECHANISM AND ANALYSIS METHODS FOR SPIN RELAXATION

Through studying the relations between  $\tau_s$  and important electronic quantities, switching on/off certain dynamic processes, or tuning the key factors affecting spin dynamics, our FPDM method is a powerful technique to determine spin relaxation mechanism and quantitatively predict spin lifetime in different materials at various conditions.

There are several mechanisms causing spin relaxation and dephasing of electron carriers in non-magnetic systems[7, 8]. Among them, the most important mechanisms are Elliot-Yafet (EY) and Dyakonov-Perel (DP) mechanisms. EY represents spin relaxation due to spin-flip scattering. DP is activated when inversion symmetry is broken, which results in random spin precession between adjacent scattering events. Similar to DP mechanism, free induction decay (FID) mechanism is caused

by random spin precession but happens when scattering is weak enough. Below we show how to determine spin relaxation mechanism and analyse spin relaxation through *ab-initio* simulations. We note that our FPDM approach provides unified treatment for different mechanisms. We also acknowledge that some approximate models were proposed in the past specific for each mechanism, which was helpful for providing mechanistic insights and qualitative understanding. We will introduce them in the following sections. By comparing FPDM and these approximate models, we can further grasp the detailed physical picture of spin relaxation.

### A. Spin expectation value, spin texture and internal magnetic field

We first define some important spin-related properties in spin dynamics.

The spin expectation value along  $i$  direction is defined as the diagonal element of spin matrix  $s_i$ , i.e.,

$$S_{i,1}^{\text{exp}} = s_{i,11}. \quad (57)$$

Note that for degenerate bands, the matrix elements of  $s_i$  are arbitrary, thus, we need to diagonalize  $s_i$  matrix in degenerate subspaces.

The spin texture presents when the spin up and down degeneracy (Kramers pair) is lifted (e.g., due to broken inversion symmetry), and is the distribution of the spin expectation value vector  $\mathbf{S}^{\text{exp}} \equiv (S_x^{\text{exp}}, S_y^{\text{exp}}, S_z^{\text{exp}})$ .

Suppose originally a system has time-reversal and inversion symmetries, so that every two bands form a Kramers degenerate pair. Suppose the  $\mathbf{k}$ -dependent spin matrix vectors in Bloch basis of the Kramers degenerate pairs are  $\mathbf{s}_k^0$  with  $\mathbf{s} \equiv (s_x, s_y, s_z)$ . The inversion symmetry broken induces  $\mathbf{k}$ -dependent Hamiltonian terms[7]

$$H_k^{\text{ISB}} = \mu_B g_0 \mathbf{B}_k^{\text{in}} \cdot \mathbf{s}_k^0, \quad (58)$$

where  $\mathbf{B}_k^{\text{in}}$  is the so-called internal magnetic fields at presence of SOC.  $\mathbf{B}_k^{\text{in}}$  splits the degenerate pair and polarizes the spin along its direction. The definition of  $\mathbf{B}_k^{\text{in}}$  is

$$\mathbf{B}_k^{\text{in}} \equiv 2\Delta_k \mathbf{S}_k^{\text{exp}} / (\mu_B g_0), \quad (59)$$

where  $\Delta$  is the band splitting energy. From Eq. 59,  $\mathbf{S}_k^{\text{exp}} \parallel \mathbf{B}_k^{\text{in}}$  (internal magnetic field  $\mathbf{B}_k^{\text{in}}$  is along the spin texture direction  $\mathbf{S}_k^{\text{exp}}$ ).

### B. Elliot-Yafet (EY) mechanism

EY mechanism dominates spin relaxation when spin-up and spin-down are well defined (in absence of spin precession), so that it dominates in two types of systems:

(i) Materials with both time-reversal and spatial inversion symmetries, e.g., silicon, free-standing graphene in absence of external fields. With such symmetries, every two bands form a Kramers degenerate pair[7]. Therefore, spin-up/down is well defined along an axis  $\hat{\mathbf{r}}$  by diagonalizing the corresponding spin matrix  $s_{\mathbf{r}} = \mathbf{s} \cdot \hat{\mathbf{r}}$  in degenerate subspaces. (ii) Systems with high spin polarization e.g. due to intrinsic magnetization or spin-valley locking, e.g., ferromagnets, transition metal dichalcogenides (TMDs).

#### 1. Fermi's golden rule (FGR)

*1.1 FGR with spin-flip transitions* According to Ref. [17], if a solid-state system is close to equilibrium (but not at equilibrium) and its spin relaxation is dominated by EY mechanism, its free carriers'  $\tau_s$  due to spin-orbit coupling and e-ph scattering approximately satisfies (for simplicity the band indices are dropped)

$$\tau_s^{-1} \propto \frac{N_k^{-2}}{\chi} \sum_{kq\lambda} \left\{ \begin{array}{c} |g_{k,k-q}^{\uparrow\downarrow,q\lambda}|^2 n_{q\lambda} f_{k-q}^{\text{eq}} (1 - f_k^{\text{eq}}) \\ \delta(\epsilon_k - \epsilon_{k-q} - \omega_{q\lambda}) \end{array} \right\}, \quad (60)$$

$$\chi = N_k^{-1} \sum_k f_k^{\text{eq}} (1 - f_k^{\text{eq}}), \quad (61)$$

where  $g^{\uparrow\downarrow}$  is the spin-flip e-ph matrix element between two electronic states of opposite spins,  $n_{q,\lambda}$  is phonon occupation at momentum  $q$  and mode  $\lambda$ , and  $f^{\text{eq}}$  is Fermi-Dirac distribution function. We will further discuss  $g^{\uparrow\downarrow}$  in the next subsection.

According to Eq. 60 and 61,  $\tau_s^{-1}$  is proportional to  $|g_q^{\uparrow\downarrow}|^2$  and also the density of the spin-flip transitions. Therefore we propose a temperature ( $T$ ) and chemical potential ( $\varepsilon_{\mu_F}$ ) dependent effective modulus square of the spin-flip e-ph matrix element  $|\overline{g}^{\uparrow\downarrow}|^2$  and a scattering density of states  $D^S$  as

$$|\overline{g}^{\uparrow\downarrow}|^2 = \frac{\sum_{kq} w_{k,k-q} \sum_{\lambda} |g_{k,k-q}^{\uparrow\downarrow,q\lambda}|^2 n_{q\lambda}}{\sum_{kq} w_{k,k-q}}, \quad (62)$$

$$D^S = \frac{N_k^{-2} \sum_{kq} w_{k,k-q}}{N_k^{-1} \sum_k f_k^{\text{eq}} (1 - f_k^{\text{eq}})}, \quad (63)$$

$$w_{k,k-q} = f_{k-q}^{\text{eq}} (1 - f_k^{\text{eq}}) \delta(\epsilon_k - \epsilon_{k-q} - \omega_c), \quad (64)$$

where  $\omega_c$  is the characteristic phonon energy chosen as the averaged energy of the phonons contributing to spin relaxation, and  $w_{k,k-q}$  is the weight function. The matrix element modulus square is weighted by  $n_{q\lambda}$  according to Eq. 60 and 61. This rules out high-frequency phonons at low  $T$  which are not excited.  $w_{k,k-q}$  selects transitions between states separated by  $\omega_c$  and around the band edge or  $\varepsilon_{\mu_F}$ , which are "more relevant" transitions to spin relaxation.

$D^S$  can be regarded as an effective density of spin-flip e-ph transitions satisfying energy conservation between one state and its pairs. When  $\omega_c = 0$ , we



have  $D^S = \int d\epsilon \left(-\frac{df^{\text{eq}}}{d\epsilon}\right) D^2(\epsilon) / \int d\epsilon \left(-\frac{df^{\text{eq}}}{d\epsilon}\right) D(\epsilon)$  with  $D(\epsilon)$  density of electronic states (DOS). So  $D^S$  can be roughly regarded as a weighted-averaged DOS with weight  $\left(-\frac{df^{\text{eq}}}{d\epsilon}\right) D(\epsilon)$ .

With  $|\overline{g^{\uparrow\downarrow}}|^2$  and  $D^S$ , we have the approximate relation for spin relaxation rate,

$$\tau_s^{-1} \propto |\overline{g^{\uparrow\downarrow}}|^2 D^S. \quad (65)$$

We can similarly define an effective spin conserving matrix element  $|\overline{g^{\uparrow\uparrow}}|^2$  by replacing  $g_{k,k-q}^{\uparrow\downarrow,q\lambda}$  to  $g_{k,k-q}^{\uparrow\uparrow,q\lambda}$  in Eq. 62. Then we have the approximate relation for carrier relaxation rate due to e-ph scattering,

$$\langle \tau_p^{-1} \rangle \propto |\overline{g^{\uparrow\uparrow}}|^2 D^S. \quad (66)$$

Although such formula are not as general and accurate as our FPDM formulation, Eq. 65 and 66 can be used to understand the spin flip and spin conserving e-ph matrix element's relation to spin or carrier relaxation, and one can develop intuition on what type of phonons contribute more to  $|\overline{g^{\uparrow\uparrow}}|^2$  or  $|\overline{g^{\uparrow\downarrow}}|^2$ . As our recent studies show Frölich LO phonon strongly contributes to carrier relaxation in CsPbBr<sub>3</sub>, but much less important in its spin relaxation due to the spin-conserving nature of long-ranged Frölich electron-phonon coupling [18].

**1.2 Generalized FGR** In centrosymmetric systems with strong spin-mixing and band degeneracy,  $\mathbf{S}_k^{\text{exp}}$  may have multiple values. For example, valence bands of silicon at  $\Gamma$  are four-fold degenerate and their  $\mathbf{S}_k^{\text{exp}}$  are (more precisely, very close to)  $\pm 1/2$  and  $\pm 1/6$ . In such cases, spin relaxation may be still driven by EY mechanism but needs a generalized FGR formula[17] beyond spin-flip transition,

$$\tau_{s,i}^{-1} \propto \frac{N_k^{-2}}{\chi_i} \sum_{12\lambda} \left\{ \frac{|\Delta S_{i,12}^{\text{exp},q,\lambda}|^2 n_{q\lambda}}{f_2^{\text{eq}}(1-f_1^{\text{eq}})\delta(\epsilon_1-\epsilon_2-\omega_{q\lambda})} \right\}, \quad (67)$$

$$\chi_i = N_k^{-1} \sum_1 f_1^{\text{eq}}(1-f_1^{\text{eq}}) S_{i,1}^{\text{exp},2}, \quad (68)$$

$$\Delta S_{i,12}^{\text{exp}} = S_{i,1}^{\text{exp}} - S_{i,2}^{\text{exp}}, \quad (69)$$

where  $\Delta S^{\text{exp}}$  is the change of spin expectation value for a pair of electronic states. Therefore, the transitions with non-negligible  $\Delta S^{\text{exp}}$  can contribute to spin relaxation. Again, unlike our FPDM method, this is approximate formula, which can be used to understand how e-ph scattering between a pair of states changes spin expectation value as we showcase bulk Si hole spin relaxation in Ref. 17.

## 2. Spin-mixing parameter $b^2$

**2.1 State-resolved  $b^2$ .** Suppose the spin of a state “1” is highly polarized along  $i$  direction. Then in general,

the wavefunction of state “1” can be written as  $\Psi_1(\mathbf{r}) = a_{i,1}(\mathbf{r})\alpha + b_{i,1}(\mathbf{r})\beta$ , where  $a$  and  $b$  are the coefficients of the large and small components of the wavefunction, and  $\alpha$  and  $\beta$  are spinors (one up and one down for direction  $i$ ). Define  $a_{i,1}^2 = \int |a_{i,1}(\mathbf{r})|^2 d\mathbf{r}$  and  $b_{i,1}^2 = \int |b_{i,1}(\mathbf{r})|^2 d\mathbf{r}$ , then  $a_{i,1}^2 > b_{i,1}^2$  and  $b_{i,1}^2$  is just spin-mixing parameter of state “1” along direction  $i$  [19].

$$a_{i,1}^2 + b_{i,1}^2 = 1, \quad (70)$$

$$0.5(a_{i,1}^2 - b_{i,1}^2) = S_{i,1}^{\text{exp}}, \quad (71)$$

Therefore,

$$b_{i,1}^2 = 0.5 - S_{i,1}^{\text{exp}}. \quad (72)$$

**2.2 EY relation.** According to Eq. 60 and 66, we have

$$\tau_s^{-1}/\tau_p^{-1} \propto |\overline{g^{\uparrow\downarrow}}|^2/|\overline{g^{\uparrow\uparrow}}|^2, \quad (73)$$

where  $\tau_p = 1/\langle \tau_p^{-1} \rangle$ .

As thermal averaging frequently appears in spin relaxation analysis, we define  $\langle A \rangle$  as the thermal average of electronic quantity  $A$ ,

$$\langle A \rangle = \frac{\sum_{kn} (-[f^{\text{eq}}]_{kn}') A_{kn}}{\sum_{kn} (-[f^{\text{eq}}]_{kn}')}, \quad (74)$$

where  $[f^{\text{eq}}]'$  is the derivative of the Fermi-Dirac distribution function.

According to Refs. 9, 65, 66,  $|\overline{g^{\uparrow\downarrow}}|^2/|\overline{g^{\uparrow\uparrow}}|^2 \sim \langle b^2 \rangle$ , so that

$$\tau_s^{-1}/\tau_p^{-1} \sim \langle b^2 \rangle. \quad (75)$$

The above is a rough relation and cannot be used to predict  $\tau_s$  (the error may be several or even ten times). Practically, we use the following approximate relation

$$\tau_s^{-1}/\tau_p^{-1} = 4 \langle b^2 \rangle. \quad (76)$$

This is called EY relation in this work.

## 3. Spin-flip angle $\theta^{\uparrow\downarrow}$

In our previous paper[21], we proposed an important electronic quantity for intervalley spin-flip scattering - the spin-flip angle  $\theta^{\uparrow\downarrow}$  between two electronic states. For two states  $(k, n)$  and  $(k', n')$  with opposite spin directions,  $\theta^{\uparrow\downarrow}$  is the angle between  $-\mathbf{S}_{kn}^{\text{exp}}$  and  $\mathbf{S}_{k'n'}^{\text{exp}}$ . The motivation of examining  $\theta^{\uparrow\downarrow}$  is that: According to Ref. [67], due to time-reversal symmetry, the spin-flip matrix element of the same band between  $\mathbf{k}$  and  $-\mathbf{k}$  is exactly zero, so that  $g^{\uparrow\downarrow}$  is zero at lowest order for intervalley transitions between two opposite valleys (e.g.,  $\mathbf{K}$  and  $-\mathbf{K}$ ). In the first-order perturbation level,  $|g^{\uparrow\downarrow}|$  between

two states is determined by  $\theta^{\uparrow\downarrow}$  between these two states and proportional to  $|\sin(\theta^{\uparrow\downarrow}/2)|$ .

Suppose (i) the inversion symmetry broken induces  $\mathbf{B}_k^{\text{in}}$  (Eq. 59) for a Kramers degenerate pair; (ii) there are two valleys centered at wavevectors  $\mathbf{Q}$  and  $-\mathbf{Q}$  and (iii) there are two wavevectors  $\mathbf{k}_1$  and  $\mathbf{k}_2$  near  $\mathbf{Q}$  and  $-\mathbf{Q}$  respectively. Due to time-reversal symmetry, the directions of  $\mathbf{B}_{k_1}^{\text{in}}$  and  $\mathbf{B}_{k_2}^{\text{in}}$  are almost opposite.

We can prove that for a general operator  $\hat{A}$ ,

$$|A_{k_1 k_2}^{\uparrow\downarrow}|^2 \approx \sin^2(\theta_{k_1 k_2}^{\uparrow\downarrow}/2) |A_{k_1 k_2}^{\downarrow\downarrow}|^2, \quad (77)$$

where  $A_{k_1 k_2}^{\uparrow\downarrow}$  and  $A_{k_1 k_2}^{\downarrow\downarrow}$  are the spin-flip and spin-conserving matrix elements between  $\mathbf{k}_1$  and  $\mathbf{k}_2$  respectively. We present the detailed derivation in SI Sec. SIII of Ref. 21.

From Eq. 77, for the intervalley e-ph matrix elements, we have

$$|g_{k_1 k_2}^{\uparrow\downarrow}|^2 \approx \sin^2(\theta_{k_1 k_2}^{\uparrow\downarrow}/2) |g_{k_1 k_2}^{\downarrow\downarrow}|^2. \quad (78)$$

Finally, similar to Eq. 62, we propose an effective modulus square of  $\sin^2(\theta_{k_1 k_2}^{\uparrow\downarrow}/2)$ ,

$$\frac{1}{\sin^2(\theta^{\uparrow\downarrow}/2)} = \frac{\sum_{kq} w_{k,k-q} \sin^2(\theta_{k,k-q}^{\uparrow\downarrow}/2)}{\sum_{kq} w_{k,k-q}}. \quad (79)$$

We found spin relaxation time (obtained from our FPDM method) linearly proportional to this quantity ( $\sin^2(\theta^{\uparrow\downarrow}/2)$ ) when intervalley spin relaxation process dominates, as an example of substrate effects on spin relaxation of strong SOC Dirac materials in Ref. 21. Such angle relates to the spin expectation value direction between initial  $\uparrow$  and final  $\downarrow$  states.

### C. Dyakonov-Perel (DP) and Free induction decay (FID) mechanisms

#### 1. Model relations

For non-magnetic materials, with nonzero k-dependent internal magnetic field  $\mathbf{B}_k^{\text{in}}$  induced by inversion symmetry broken and spin-orbit coupling, the spins at  $\mathbf{k}$  precess about  $\mathbf{B}_k^{\text{in}}$ . The Larmor precession frequency vector can be defined as:

$$\mathbf{\Omega}_k = \Delta_k \hat{\mathbf{S}}_k^{\text{exp}}, \quad (80)$$

where  $\hat{\mathbf{S}}_k^{\text{exp}}$  is the normalized  $\mathbf{S}_k^{\text{exp}}$ .

We define  $\mathbf{\Omega}_{\perp\hat{\mathbf{r}}}$  as the component of  $\mathbf{\Omega}$  perpendicular to direction  $\hat{\mathbf{r}}$ . Suppose the fluctuation amplitude among

different k-points of  $\mathbf{\Omega}_{\perp\hat{\mathbf{r}}}$  is  $\Delta\mathbf{\Omega}_{\perp\hat{\mathbf{r}}}$  and numerically we define it as (using Eq. 74)

$$\Delta\mathbf{\Omega}_{\perp\hat{\mathbf{r}}} = \sqrt{\langle |\mathbf{\Omega}_{\perp\hat{\mathbf{r}}} - \langle \mathbf{\Omega}_{\perp\hat{\mathbf{r}}} \rangle|^2 \rangle}. \quad (81)$$

According to Refs. 7 and 8, a nonzero  $\Delta\mathbf{\Omega}$  leads to finite spin lifetime  $\tau_s^{\Delta\mathbf{\Omega}}$  along  $\hat{\mathbf{r}}$  and the spin relaxation mechanism depends on the magnitude of  $\tau_p \Delta\mathbf{\Omega}$ [7, 8] (the subindex “ $\perp\hat{\mathbf{r}}$ ” is dropped for simplicity):

(i) DP mechanism if  $\tau_p \Delta\mathbf{\Omega} \ll 1$  (strong scattering limit). We have the DP relation

$$(\tau_s^{\Delta\mathbf{\Omega}})^{-1} \sim (\tau_s^{\text{DP}})^{-1} \sim \tau_p (\Delta\mathbf{\Omega})^2. \quad (82)$$

(ii) FID mechanism if  $\tau_p \Delta\mathbf{\Omega} \gtrsim 1$  (weak scattering limit). We have

$$(\tau_s^{\Delta\mathbf{\Omega}})^{-1} \sim (\tau_s^{\text{FID}})^{-1} \sim \Delta\mathbf{\Omega}. \quad (83)$$

(iii) Between (i) and (ii) regimes, there isn't a good approximate relation for  $(\tau_s^{\Delta\mathbf{\Omega}})^{-1}$ , but we may expect that[8]

$$(\tau_s^{\text{DP}})^{-1} < (\tau_s^{\Delta\mathbf{\Omega}})^{-1} < (\tau_s^{\text{FID}})^{-1}. \quad (84)$$

#### 2. Landé g-factor of free carriers

Besides intrinsic spin-orbit coupling, one channel to induce nonzero  $\Delta\mathbf{\Omega}$  is through  $g$  factor fluctuations under magnetic field. In Sec. II A 2, we have described how  $\mathbf{B}^{\text{ext}}$  is considered in FPDM approach, therefore, with  $H_z(\mathbf{B}^{\text{ext}})$ , the magnetic-field effects on spin dynamics are straightforwardly included in FPDM simulations.

For the description of the magnetic-field effects, Landé  $g$ -factor has been widely used[18]. For a single band and a pair of bands,  $g$ -factor is well defined and relates to  $\mathbf{B}^{\text{ext}}$ -induced change of energy, energy splitting and/or Larmor precession frequency. In this work, we limit our discussions to two Kramers degenerate bands under a transverse  $\mathbf{B}^{\text{ext}}$  (perpendicular to the direction of the excess/excited spin  $\mathbf{S} \equiv (S_x, S_y, S_z)$ ). In general, in the two-band case,  $g$ -factor is a tensor and may be defined by the relation  $\mathbf{\Omega}_k(\mathbf{B}^{\text{ext}}) = \mu_B \mathbf{B}^{\text{ext}} g_k^S$ . Here, for simplicity, we assume  $\mathbf{\Omega}_k(\mathbf{B}^{\text{ext}}) \parallel \mathbf{B}^{\text{ext}}$ , which is valid in many materials including CsPbBr<sub>3</sub>. With this assumption and from Eq. 80,

$$g_k^S = \frac{\mathbf{\Omega}_k(\mathbf{B}^{\text{ext}}) \cdot \hat{\mathbf{B}}^{\text{ext}}}{\mu_B B^{\text{ext}}}. \quad (85)$$

$\mathbf{\Omega}_k(\mathbf{B}^{\text{ext}})$  is computed using Eq. 80.

However, in many previous theoretical studies[68, 69],  $g$ -factors were defined based on pseudo-spins related to the total magnetic momenta  $J^{\text{at}}$ , which are determined from the atomic-orbital models. The pseudo-spins can have opposite directions to the actual spins ( $S$ ). Most

previous experimental studies adopted the same convention for the signs of carrier  $g$ -factors. Therefore, to compare with  $g$ -factors obtained in those previous studies, we introduce a correction factor  $C^{S \rightarrow J}$  and define a new  $g$ -factor:

$$\tilde{g}_k \left( \widehat{\mathbf{B}}^{\text{ext}} \right) = C^{S \rightarrow J} g_k^S. \quad (86)$$

$C^{S \rightarrow J} = m_S^{\text{at}}/m_J^{\text{at}}$  with  $m_J^{\text{at}}$  and  $m_S^{\text{at}}$  the total and spin magnetic momenta respectively, obtained from the atomic-orbital model[69].  $C^{S \rightarrow J}$  is independent from  $\mathbf{k}$ -point, and is  $\mp 1$  for electrons and holes respectively for CsPbBr<sub>3</sub> [18].

As  $\tilde{g}_k$  is different at different  $\mathbf{k}$ , we can define its fluctuation amplitude as

$$\Delta \tilde{g} = \left\langle (\tilde{g} - \langle \tilde{g} \rangle)^2 \right\rangle. \quad (87)$$

From the above equation, we have the fluctuation amplitude of  $\Omega_k(\mathbf{B}^{\text{ext}})$

$$\Delta \Omega(\mathbf{B}^{\text{ext}}) = \mu_B B^{\text{ext}} \Delta \tilde{g}. \quad (88)$$

A nonzero  $\Delta \Omega(\mathbf{B}^{\text{ext}})$  leads to spin dephasing under external magnetic field  $\mathbf{B}^{\text{ext}}$  and the mechanism may be DP or FID depending on the magnitude of  $\tau_p \Delta \Omega$  as discussed above.

## D. Determination of spin relaxation mechanism

In general, the applicability of our FPDM approach does not depend on specific spin relaxation mechanism. To determine the dominant relaxation or dephasing mechanism, we have the following two approaches by utilizing our FPDM calculations.

### 1. Method 1: Comparing FPDM calculations with FGR or model relations

The first approach is to compare FPDM results directly with simple models designed for various mechanisms as introduced in previous two sections. If FPDM agrees with one of the model relations, it is a good indicator of dominant mechanism.

*1.1 EY mechanism.* Since spin precession is suppressed when EY mechanism dominates, the DM master equation in semiclassical limit from Eq. 49 and FGR formula with spin-flip scattering Eq. 60 should describe well spin relaxation (suppose spin matrix is diagonalized in degenerate subspaces along the direction of the excess spin). Therefore, if the values and trends of  $\tau_s$  by Eq. 49 and 60 are similar to those obtained from FPDM calculations, the dominating mechanism is likely the EY.

*1.2 DP or FID mechanism.* With nonzero  $\Delta \Omega$ , whether spin relaxation is dominated by DP or FID mechanism may be determined by comparing the values and trends of  $\tau_s$  by Eq. 82 or 83 with the FPDM results. We have shown the success of such analysis in our previous work on spin relaxation and transport in germanene and silicene under electric field [19] as well as CsPbBr<sub>3</sub> under magnetic field [18].

### 2. Method 2: Tuning the scattering strength or precession frequency in FPDM calculations

Conventionally, spin relaxation mechanism is determined from the relation between  $\tau_s$  and  $\tau_p$  - EY mechanism leads to  $\tau_s \propto \tau_p$  while DP mechanism leads to  $\tau_s \propto \tau_p^{-1}$ . Another way to look at this is through tuning the strength of scatterings (e.g. physically, increasing impurity concentration increases scattering). If  $\tau_s$  decreases with increasing scattering, it's likely EY; otherwise, it's likely DP mechanism, because  $\tau_p$  always decreases with increasing scatterings.

Practically in our FPDM calculations, this approach can be implemented by introducing a scaling factor  $F^{\text{sc}}$  to tune the scattering strength, i.e. multiplying  $F^{\text{sc}}$  to the scattering term  $\frac{d\rho}{dt}|_{\text{scatt}}$  of the DM master equation (Eq. 5) but keep the coherent term (the first term of Eq. 5) unchanged. This is equivalent to multiply  $F^{\text{sc}}$  to all elements of the generalized scattering-rate matrix  $P$  (Eq. 18, 21 and 25).

To avoid confusions, we name carrier and spin lifetimes after introducing  $F^{\text{sc}}$  as  $\tau'_s$  and  $\tau'_p$  respectively. According to Eq. 51, we always have  $\tau'_p/\tau_p = (F^{\text{sc}})^{-1}$ . On the other hand,  $\tau'_s$  depends on the spin relaxation mechanism. For EY mechanism,  $\tau'_s/\tau'_p = \tau_s/\tau_p = C^{\text{EY}}$ , where  $C^{\text{EY}}$  is a constant unrelated to  $F^{\text{sc}}$ . Therefore, it can be proven that  $\tau'_s/\tau_s = (F^{\text{sc}})^{-1} = \tau'_p/\tau_p$ . Similarly, for DP mechanism, we can prove that  $\tau'_s/\tau_s = F^{\text{sc}} = (\tau'_p/\tau_p)^{-1}$ . For FID mechanism, as  $\tau'_s$  is irrelevant to  $\tau'_p$ , we have  $\tau'_s/\tau_s \equiv 1$ . Therefore, the relation between  $\tau'_s/\tau_s$  and  $\tau'_p/\tau_p$  by tuning  $F^{\text{sc}}$  is useful to understand spin relaxation mechanism.

Moreover, the relation between  $\tau_s$  and  $\Delta \Omega$  is also useful to understand spin relaxation mechanism.  $\Delta \Omega$  can be tuned easily by tuning the energy splitting.

## IV. APPLICATIONS

### A. Non-magnetic materials with inversion symmetry

We first present results for systems with inversion symmetry traditionally described by EY mechanism. Figure 2(a) shows that our theoretical electron  $\tau_s$  of Si as a function of  $T$  are in excellent agreement with experimental measurements[70, 71]. Note that previous first-

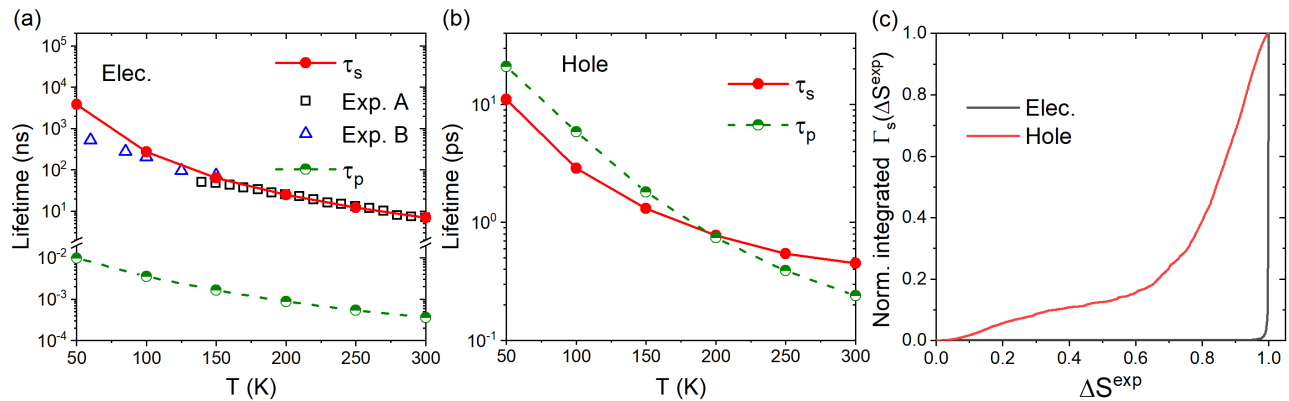


FIG. 2. Spin relaxation in Silicon (Si). Spin ( $\tau_s$ ) and carrier ( $\tau_p$ ) lifetimes of (a) electrons and (b) holes of Si. Exp. A and B are from Ref. 70 and 71. (c) Cumulative contributions to spin relaxation by change in spin,  $\Delta s$ , per scattering event defined based on Eqs. 67-69: electrons in Si exhibit spin flips with all contributions at  $\Delta s = 1$ , whereas holes in Si and electrons in iron exhibit a broad distribution in  $\Delta s$  [17].

principles calculations[9] approximated spin-flip electron-phonon matrix elements from pseudospin wavefunction overlap and spin-conserving electron-phonon matrix element, effectively assuming that the scattering potential varies slowly on the scale of a unit cell; we make no such approximation in our FPDM approach. In contrast, holes in Si exhibit strong spin mixing with spin-2/3 character and spin expectation values no longer close to  $\hbar/2$ . Figure 2(b) shows our predictions for the hole spin lifetime  $\tau_{s,h}$  which is much shorter than the electron spin as a result of the strong mixing (450 fs for holes compared to 7 ns for electrons at 300 K) and is much closer to carrier relaxation time  $\tau_p$ . Additionally, Fig. 2(c) shows that the change in spin expectation values ( $\Delta S^{\text{exp}}$ ) per scattering event (evaluated using Eqs. 67-69) has a broad distribution for holes in Si, indicating that they cannot be described purely by spin-flip transitions, while conduction electrons in Si predominantly exhibit spin-flip transitions with  $\Delta S^{\text{exp}} = 1$ .

## B. Materials with high spin polarization

In ferromagnets and antiferromagnets, spins are highly polarized, so that spin relaxation is likely dominated by EY mechanism. In Ref. 17, we simulated  $\tau_s$  of bcc iron, where we found good agreement with experiments, with a dominant EY mechanism (magnon was not considered here). In nonmagnetic materials, when inversion symmetry is broken and SOC strength is moderate or large, it has been found that some of them such as transition metal dichalcogenides also have highly polarized carrier spins and exhibit EY spin relaxation.

### 1. Transition metal dichalcogenides (TMDs)

Monolayer TMDs exhibit exciting features including spin-polarized bands, valley-specific optical selection rules and spin-valley locking. In Ref. 72, 73, it has been shown that by introducing doping in monolayer TMDs, ultraslow decays of Kerr rotations, which correspond to ultralong spin/valley lifetimes of resident carriers especially resident holes, can be observed at low temperatures. Those features establish TMDs' advantages for spin-valleytronics and (quantum) information processing. Although spin/valley relaxation time of resident carriers in monolayer TMDs, most relevant to spinvalleytronics' application, has been extensively examined, the underlying relaxation mechanisms especially the effects of different types of impurities have not been addressed through *ab-initio* simulations.

In Ref. 16, we clarified the above problem by conducting *ab initio* real-time dynamics simulations with relevant scattering mechanisms. We focused on WSe<sub>2</sub> due to its larger valence band SOC splitting and weaker interlayer coupling compared with other TMDs and focused on dynamics of resident holes as  $\tau_s$  of holes seem longer than electrons.

For holes of monolayer WSe<sub>2</sub>, spin/valley relaxation is completely determined by intervalley spin-flip scattering between  $K$  and  $K'$  valleys because of spin-valley locking. Previously, we reported spin/valley lifetimes of resident holes of monolayer TMDs at  $T \geq 50$  K with e-ph scattering[17]. At very low temperatures, e.g., 10 K, intervalley e-ph scattering is however not activated as the corresponding phonon occupation is negligible, so that other scattering mechanisms need to be included. Note that e-e scattering should not play an important role in spin relaxation of holes of TMDs. The reason is: The e-e scattering is a two-particle process where a transition is accompanied by another transition with energy and momentum being conserved. Considering the fact that

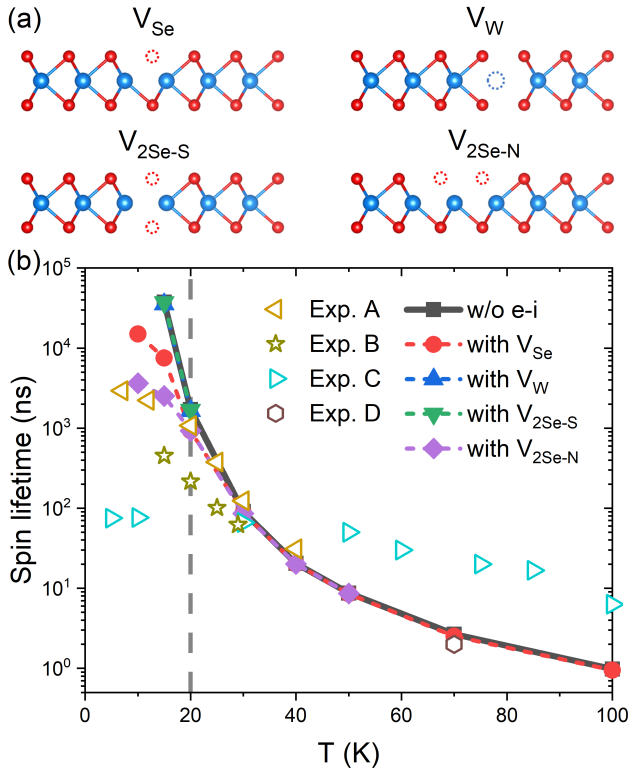


FIG. 3. (a) The schematics of four types of impurities in  $\text{WSe}_2$ . (b) Spin lifetimes of holes of monolayer  $\text{WSe}_2$  with a relatively low hole density  $10^{11} \text{ cm}^{-2}$  with impurities compared with experimental data[73–76]. The choices of impurity concentration  $n_i$  of different impurities are given in the main text [16].

only the highest occupied band is involved in dynamics of TMD holes, for a e-e process, a  $K \rightarrow K'$  ( $K' \rightarrow K$ ) spin-flip transition must be accompanied by an opposite  $K' \rightarrow K$  ( $K \rightarrow K'$ ) spin-flip transition. Overall, an e-e scattering process cannot change the spin of the system. Therefore, we will include only e-ph and e-i scatterings.

Experimentally there exists many types of impurities/defects in TMD samples. Here we pick four types of impurities with different symmetries and chemical bonds (see Fig. 3(a)) - Se vacancy (Se vac.), two neighboring Se vacancies (2N-Se vac.), W vacancy (W vac.) and two Se vacancies with the same in-plane position (2S-Se vac.). According to Refs. 77–79,  $n_i$  ranges from  $8 \times 10^{10}$  to  $10^{14} \text{ cm}^{-2}$  depending on samples. Considering that Se vac. is often regarded as the most abundant impurity, we choose a reasonable  $n_i$  of Se vac. -  $7 \times 10^{11} \text{ cm}^{-2}$ , which is taken relatively low for better comparison with experimental  $\tau_s$  shown in Fig. 3(b). Since the formation energy of Se vac. seems lowest and  $n_i$  of larger impurities are found lower than smaller impurities[79],  $n_i$  of 2N-Se vac. is chosen as  $8 \times 10^9 \text{ cm}^{-2}$  lower than Se vac. and also for better comparison with experimental  $\tau_s$ .  $n_i$  of W vac. and 2S-Se vac. are chosen arbitrarily as we found they have rather weak effects on spin relaxation and are  $7 \times 10^{11}$  and  $3.5 \times 10^{11} \text{ cm}^{-2}$ , respectively.

From Fig. 3, we first find that assuming  $n_i$  not so high, at  $T > 20 \text{ K}$ , spin relaxation is almost driven by e-ph scattering and impurities can only affect spin relaxation at  $T \leq 20 \text{ K}$ . For the effects on spin relaxation of different impurities, we have  $2\text{N-Se vac.} \gg \text{Se vac.} \gg \text{W vac.} \sim 2\text{S-Se vac.}$ . Moreover, the temperature dependence of  $\tau_s$  with 2N-Se vac. is much weaker and in better agreement with experiments than that with Se vac.. Therefore, the observed weak temperature dependence in some experiments is probably related the existence of larger impurities with lower symmetries. Our observations suggest that the local symmetry and chemical bonds surround a impurity have large impact on spin relaxation. To understand why the effects of different impurities on spin relaxation significantly differ, further theoretical investigations on how impurities affect impurity potentials and their SOC corrections are required.

## 2. Germanene under an electric field or on a substrate

In Ref. 19, through FPDM simulations, we predicted that monolayer germanene (ML-Ge) has giant spin lifetime anisotropy, spin-valley-locking (SVL) effect under nonzero perpendicular electric field  $E_z$  and long  $\tau_s$  ( $\sim 100 \text{ ns}$  at  $50 \text{ K}$ ), which makes it advantageous for spin-valleytronic applications. In 2D-material-based spintronic devices, the materials are usually supported on a substrate. Therefore, for the design of those devices, it is crucial to understand substrate effects on spin relaxation. We further examined  $\tau_s$  of ML-Ge on different substrates in Ref. 21.

We show band structures and spin textures of free-standing and supported ML-Ge in Fig. 4, which are essential for understanding spin relaxation mechanisms. At  $E_z = 0$ , ML-Ge has time-reversal and inversion symmetries, so that its bands are Kramers degenerate[7]. A finite  $E_z$  or a substrate breaks the inversion symmetry and induces a strong out-of-plane  $\mathbf{B}^{\text{in}}$  (and also  $\mathbf{S}^{\text{exp}}$ , Eq. 59), which splits the Kramers pairs into spin-up and spin-down bands[19]. Interestingly, we find that band structures of ML-Ge-SiH (Fig. 4c) and ML-Ge-GeH (not shown) are quite similar to free-standing ML-Ge under  $E_z = -7 \text{ V/nm}$  (ML-Ge@-7V/nm, Fig. 4b), which indicates that the impact of the SiH/GeH substrate on band structure (and also  $\mathbf{B}^{\text{in}}$ ) may be similar to a finite  $E_z$ . This similarity is frequently assumed in model Hamiltonian studies[80, 81]. On the other hand, the band structures of ML-Ge-InSe (Fig. 4d) and ML-Ge-GaTe (not shown) have more differences from the free-standing one under  $E_z$ , with larger band gaps, smaller band curvatures at Dirac Cones, and larger electron-hole asymmetry of band splittings. This implies that the impact of the InSe/GaTe substrates can not be approximated by applying an  $E_z$  to the free-standing ML-Ge, unlike SiH/GeH substrates. We further examine  $\mathbf{S}^{\text{exp}}$  of substrate-supported ML-Ge. Importantly, from Fig. 4e and 4f, although  $\mathbf{S}^{\text{exp}}$  of ML-Ge on substrates are highly

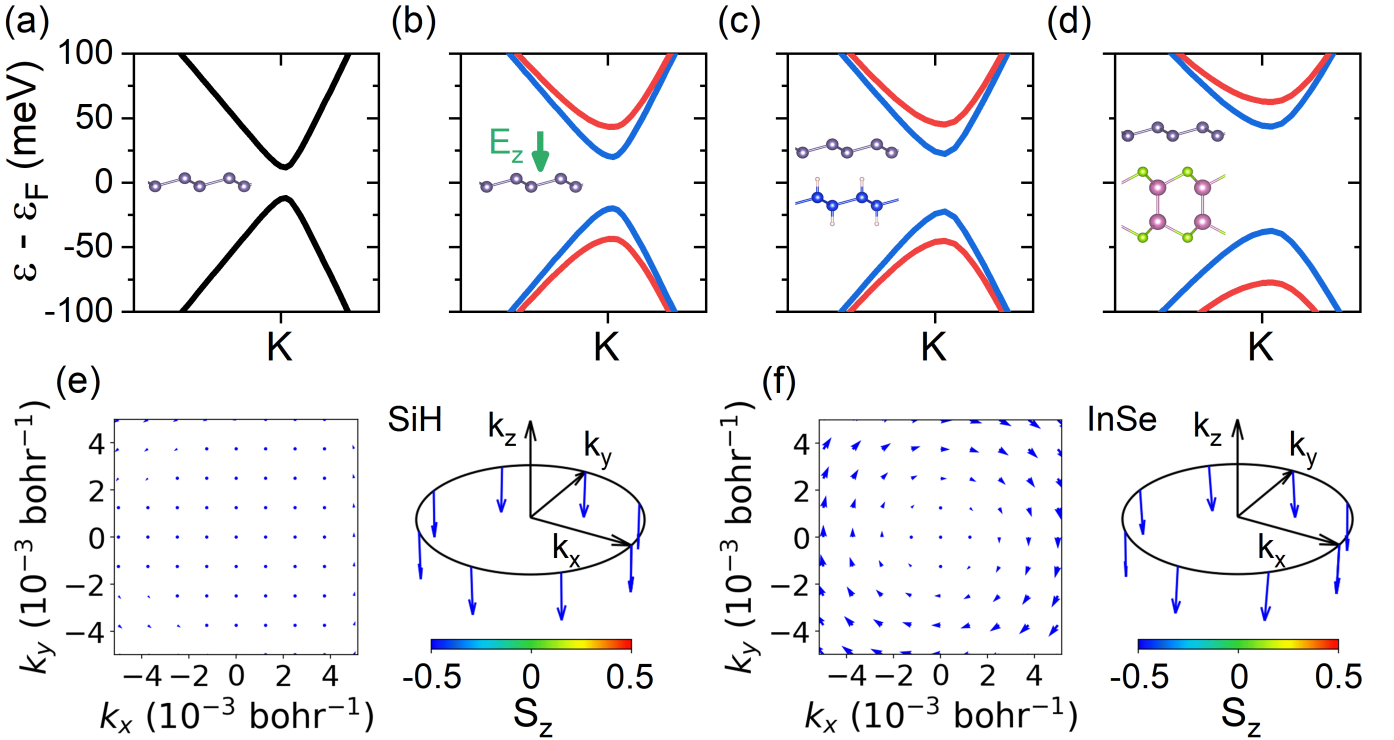


FIG. 4. Band structures and spin textures around the Dirac cones of ML-Ge systems with and without substrates. (a)-(d) show band structures of ML-Ge under  $E_z = 0$  and under  $-7$  V/nm and ML-Ge on silicane (SiH) and on InSe substrates respectively. The red and blue bands correspond to spin-up and spin-down states. Due to time-reversal symmetry, band structures around another Dirac cone at  $K' = -K$  are the same except that the spin-up and spin-down bands are reversed. The grey, white, blue, pink and green balls correspond to Ge, H, Si, In and Se atoms, respectively. Band structures of ML-Ge on germanane (GeH) and GaTe are shown in Supplementary Figure 4 in the Supporting Information, and are similar to those of ML-Ge on SiH and InSe substrates, respectively. (e) and (f) show spin textures in the  $k_x$ - $k_y$  plane and 3D plots of the spin vectors  $\mathbf{S}_{\mathbf{k}_1}^{\text{exp}}$  on the circle  $|\mathbf{k}| = 0.005$  bohr $^{-1}$  of the band at the band edge around K of ML-Ge on SiH and InSe substrates respectively. The color scales  $S_z^{\text{exp}}$  and the arrow length scales the vector length of in-plane spin expectation value [19].

polarized along  $z$  (out-of-plane) direction, the in-plane components of  $\mathbf{S}^{\text{exp}}$  of ML-Ge-InSe (and ML-Ge-GaTe) are much more pronounced than ML-Ge-SiH (and ML-Ge-GeH). Such differences are crucial to the out-of-plane spin relaxation as discussed later.

We compare out-of-plane  $\tau_s$  due to e-ph scattering between the free-standing ML-Ge (with/without an electric field) and ML-Ge on different substrates in Fig. 5. From Fig. 5, we find that  $\tau_s$  of ML-Ge under  $E_z = 0$  and  $-7$  V/nm are at the same order of magnitude for a wide range of temperatures. The differences are only considerable at low  $T$ , e.g. by 3-4 times at 20 K. On the other hand,  $\tau_s$  of supported ML-Ge are very sensitive to the specific substrates. While  $\tau_s$  of ML-Ge-GeH and ML-Ge-SiH have the same order of magnitude as the free-standing ML-Ge, in particular very close between ML-Ge-GeH and ML-Ge@ $-7$  V/nm,  $\tau_s$  of ML-Ge-GaTe and ML-Ge-InSe are shorter by at least 1-2 orders of magnitude in the whole temperature range.

Since spins of ML-Ge at  $E_z \neq 0$  and on a substrate are highly polarized, spin relaxation in ML-Ge systems is dominated by EY mechanism caused by spin-flip scattering. According to Eq. 65 and 75,  $\tau_s^{-1}$  is roughly pro-

portional to density of states (DOS) and spin-mixing parameter  $\langle b_z^2 \rangle$ . Indeed, in Ref. 21, we find that at 300 K, the differences of  $\tau_s$  of ML-Ge on different substrates are well explained by the differences of the products of DOS and  $\langle b_z^2 \rangle$ . However, at  $T \leq 50$  K, the differences of the products of DOS and  $\langle b_z^2 \rangle$  for different substrates are about 3-7 times, while the differences of  $\tau_s$  for different substrates can be as large as two orders of magnitude. Therefore, the substrate effects on  $\tau_s$  can not be fully explained by the changes of DOS and  $\langle b_z^2 \rangle$ , in particular at relatively low  $T$ .

Since  $\tau_s^{-1} \propto |\tilde{g}^{\uparrow\downarrow}|^2 D^S$  (Eq. 65), to understand substrate effects on  $\tau_s$  at low  $T$ , we first compare  $\tau_s^{-1}$  and  $|\tilde{g}^{\uparrow\downarrow}|^2 D^S$  of different ML-Ge systems. In Ref. 21, we found that  $\tau_s^{-1}$  is almost linearly proportional to  $|\tilde{g}^{\uparrow\downarrow}|^2 D^S$  at 20 K. As the variation of  $D^S$  among ML-Ge on different substrates is at most three times, which is much weaker than the large variation of  $\tau_s^{-1}$ , this indicates that the substrate-induced change of  $\tau_s$  is mostly due to the substrate-induced change of spin-flip matrix elements.

To have deeper intuitive understanding, we then pro-



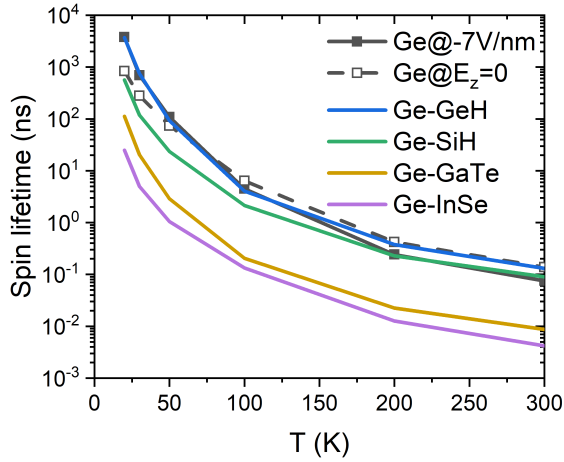


FIG. 5. The out-of-plane  $\tau_s$  of ML-Ge under  $E_z = 0, -7$  V/nm and substrate-supported ML-Ge as a function of temperature without impurities. Here we show electron  $\tau_s$  for intrinsic ML-Ge systems except that hole  $\tau_s$  is shown for ML-Ge-InSe, since electron  $\tau_s$  are longer than hole  $\tau_s$  at low  $T$  except ML-Ge-InSe [21].

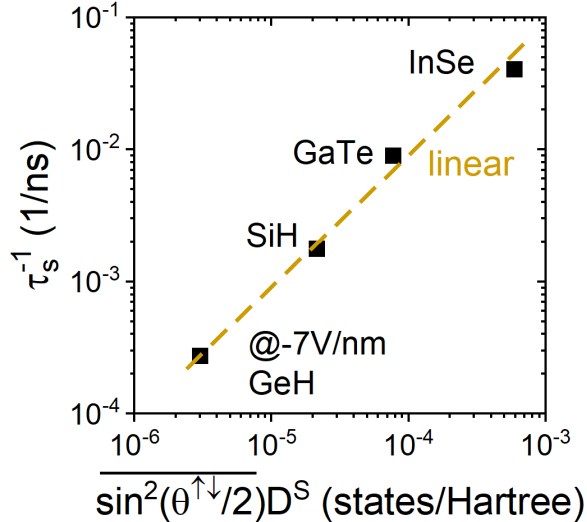


FIG. 6. The relation between  $\tau_s^{-1}$  and  $\overline{\sin^2(\theta^{\uparrow\downarrow}/2)}$  multiplied by the scattering density of states  $D^S$  at 20 K.  $D^S$  is defined in 63.  $\theta^{\uparrow\downarrow}$  is the spin-flip angle between two electronic states. For two states  $(k, n)$  and  $(k', n')$  with opposite spin directions,  $\theta^{\uparrow\downarrow}$  is the angle between  $-\mathbf{S}_{kn}^{\text{exp}}$  and  $\mathbf{S}_{k'n'}^{\text{exp}}$ .  $\overline{\sin^2(\theta^{\uparrow\downarrow}/2)}$  is defined in Eq. 79. The variation of  $D^S$  among different substrates is at most three times, much weaker than the variations of  $\tau_s^{-1}$  and other quantities shown here [21].

pose an important electronic quantity for intervalley spin-flip scattering - the spin-flip angle  $\theta^{\uparrow\downarrow}$  between two electronic states. For two states  $(k_1, n_1)$  and  $(k_2, n_2)$  with opposite spin directions,  $\theta^{\uparrow\downarrow}$  is the angle between  $-\mathbf{S}_{k_1 n_1}^{\text{exp}}$  and  $\mathbf{S}_{k_2 n_2}^{\text{exp}}$  or equivalently the angle between  $-\mathbf{B}_{k_1}^{\text{in}}$  and  $\mathbf{B}_{k_2}^{\text{in}}$ . At low  $T$ , due to large SOC splittings of conduction and valence bands of supported ML-Ge, intravalley spin-

flip e-ph scattering processes are forbidden, because the corresponding phonons have too high energies and are not occupied. So spin relaxation in supported ML-Ge is dominated by intervalley spin-flip e-ph scattering. Therefore,  $\theta^{\uparrow\downarrow}$  is helpful for understanding spin relaxation in supported ML-Ge.

The motivation of examining  $\theta^{\uparrow\downarrow}$  is that: Suppose two wavevectors  $\mathbf{k}_1$  and  $\mathbf{k}_2 = -\mathbf{k}_1$  are in two opposite valleys  $Q$  and  $-Q$  respectively and there is a pair of bands, which are originally Kramers degenerate but splitted by  $\mathbf{B}^{\text{in}}$ . Due to time-reversal symmetry, we have  $\mathbf{B}_{k_1}^{\text{in}} = -\mathbf{B}_{k_2}^{\text{in}}$ , which means the two states at the same band  $n$  at  $\mathbf{k}_1$  and  $\mathbf{k}_2$  have opposite spins and  $\theta^{\uparrow\downarrow}$  between them is zero. Therefore, the matrix element of operator  $\hat{A}$  between states  $(k_1, n)$  and  $(k_2, n)$  -  $A_{k_1 n, k_2 n}$  is a spin-flip one and we name it as  $A_{k_1 k_2}^{\uparrow\downarrow}$ . According to Ref. 67, with time-reversal symmetry,  $A_{k_1 k_2}^{\uparrow\downarrow}$  is exactly zero. In general, for another wavevector  $\mathbf{k}_3$  within valley  $-Q$  but not  $-\mathbf{k}_1$ ,  $A_{k_1 k_3}^{\uparrow\downarrow}$  is usually non-zero. One critical quantity that determines the intervalley spin-flip matrix element  $A_{k_1 k_3}^{\uparrow\downarrow}$  for a band within the pair introduced above is  $\theta_{k_1 k_3}^{\uparrow\downarrow}$ . Based on time-independent perturbation theory, we can prove that  $|A_{k_1 k_3}^{\uparrow\downarrow}|$  between two states is approximately proportional to  $|\sin(\theta^{\uparrow\downarrow}/2)|$ . The derivation is given in Sec. III B 3.

As shown in Figure 6c,  $\tau_s^{-1}$  of ML-Ge on different substrates at 20 K is almost linearly proportional to  $\overline{\sin^2(\theta^{\uparrow\downarrow}/2)} D^S$ , where  $\overline{\sin^2(\theta^{\uparrow\downarrow}/2)}$  is the statistically-averaged modulus square of  $\sin(\theta^{\uparrow\downarrow}/2)$ . This indicates that the relation  $\overline{|\hat{g}^{\uparrow\downarrow}|^2} \propto \overline{\sin^2(\theta^{\uparrow\downarrow}/2)}$  is nearly perfectly satisfied at low  $T$ , where intervalley processes dominate spin relaxation. We additionally examined the relation between  $\tau_s^{-1}$  and  $\overline{\sin^2(\theta^{\uparrow\downarrow}/2)} D^S$  at 300 K and found that the trend of  $\tau_s^{-1}$  is still approximately captured by the trend of  $\overline{\sin^2(\theta^{\uparrow\downarrow}/2)} D^S$ .

Since  $\theta^{\uparrow\downarrow}$  is defined by  $\mathbf{S}^{\text{exp}}$  at different states,  $\tau_s$  is highly correlated with  $\mathbf{S}^{\text{exp}}$  and more specifically with the anisotropy of  $\mathbf{S}^{\text{exp}}$  (equivalent to the anisotropy of  $\mathbf{B}^{\text{in}}$ ). Qualitatively, the larger anisotropy of  $\mathbf{S}^{\text{exp}}$  leads to smaller  $\theta^{\uparrow\downarrow}$  (consistent with Fig. 4e and f) and longer  $\tau_s$  along the high-spin-polarization direction. This finding may be applicable to spin relaxation in other materials whenever intervalley spin-flip scattering dominates or spin-valley locking exists, e.g., in TMDs[72], Stanene[82], 2D hybrid perovskites with persistent spin helix[6], etc.

### C. DP (Dyakonov-Perel) systems

In many non-magnetic materials with broken inversion symmetry, spin relaxation is dominated by DP mechanism.

## 1. GaAs

Spin dynamics in GaAs has broad interest in spintronics over past decades[7, 47, 83–85] and more recently[86–88], partly due to its long spin lifetime in n-type GaAs at low temperatures[47]. Despite various experimental [47, 48, 83, 89, 90] and theoretical [7, 84, 85, 91–93] (mostly using parameterized model Hamiltonian) studies previously, the dominant spin relaxation mechanism in bulk GaAs at various  $T$  and doping concentrations  $n_i$  remains unclear.

Through FPDM simulations of  $n$ -GaAs at various  $T$  and  $n_i$  with different scattering mechanisms in Ref. 16, we pointed out that although at low temperatures and moderate doping concentrations e-i scattering dominates carrier relaxation, e-e scattering is the most dominant process in spin relaxation. Moreover, we found that the relative contributions of phonon modes vary considerably between spin and carrier relaxation.

Figure 7 shows  $\tau_s$  and  $\tau_p$  with different  $n_i$  at 30 K with individual and total scattering pathways, respectively. It is found that the roles of different scattering mechanism differ considerably between spin and carrier relaxation processes. Specifically, for the carrier relaxation in Fig. 7b, except when  $n_i$  is very low (e.g. at  $10^{14}$  cm $^{-3}$ ), the e-i scattering dominates. On the other hand, for the spin relaxation in Fig. 7a, the e-e scattering dominates except at very high concentration (above  $10^{17}$  cm $^{-3}$ ), while e-i scattering is only important in the very high doping region (close to or above  $10^{17}$  cm $^{-3}$ ).

Figure 7 shows the calculated  $\tau_s$  has a maximum at  $n_i = 1-2 \times 10^{16}$  cm $^{-3}$ , and  $\tau_s$  decreases fast with  $n_i$  going away from its peak position. This is in good agreement with the experimental finding in Ref. 47, which also reported  $\tau_s$  at  $n_i = 10^{16}$  cm $^{-3}$  is longer than  $\tau_s$  at other lower and higher  $n_i$  at a low temperature (a few Kelvin). The  $n_i$  dependence of  $\tau_s$  may be qualitatively interpreted from the DP relation[7]  $\tau_{s,z} \sim \tau_p \Delta\Omega_{\perp z}^2$  (Eq. 82), where  $\Delta\Omega_{\perp z}$  is the fluctuation amplitude of Larmor frequency defined in Eq. 81. From Fig. 7, we find that with  $n_i$  from  $10^{14}$  cm $^{-3}$  to  $5 \times 10^{15}$  cm $^{-3}$ ,  $\tau_p$  decreases rapidly (black curve in Fig. 7b) and  $\Delta\Omega_{\perp z}^2$  remains flat in Fig. 7c, which may explain why  $\tau_s$  increases in Fig. 7a based on the DP relation; however, when  $n_i > 10^{16}$  cm $^{-3}$ ,  $\tau_p$  decreases with a similar speed but  $\Delta\Omega_{\perp z}^2$  experiences a sharp increase, which may explain why  $\tau_s$  decreases in Fig. 7b and owns a maximum at  $10^{16}$  cm $^{-3}$ .

Note that although the DP relation is intuitive to understand the cause of doping-level dependence of spin lifetime, it may break down when we evaluate individual scattering processes. For example, when  $n_i$  increases from  $10^{14}$  cm $^{-3}$  to  $10^{15}$  cm $^{-3}$ , both carrier lifetime  $\tau_s$  and  $\tau_{s,z}$  due to e-i scattering decrease while the internal magnetic field remains unchanged. Moreover, the simple empirical relation cannot possibly explain our first-principles results that the e-e and e-i scatterings have largely different contributions in carrier and spin relaxation. First-principles calculations are critical to provide

unbiased mechanistic insights to spin and carrier relaxation of general systems.

## 2. Graphene on hBN

Graphene samples exhibit exciting spintronic properties such as long  $\tau_s$  and  $l_s$  at room temperature [1, 94]. In practice, graphene is usually supported by a substrate[94–98]. Actually  $\tau_s$  of the free-standing graphene sample was found relatively low[99]  $\sim 150$  ps at 300 K (compared with the longest reported value  $\sim 12$  ns), probably due to free-standing graphene samples often have more imperfections. Therefore, it is important to understand spin relaxation in supported graphene.

From Fig. 8, we find that the EY model for graphene, and the DP model for Gr+ $E_{\perp}$  and Gr-hBN, agree qualitatively with FPDM predictions, but with some important quantitative differences discussed next. First, the EY model for graphene is more accurate for electrons than for holes, for both  $\tau_{s\parallel}$  and  $\tau_{s\perp}$  (Fig. 8(a-b)). The conventional DP model matches FPDM predictions quantitatively for both  $\tau_{s\parallel}$  and  $\tau_{s\perp}$  of Gr+ $E_{\perp}$ , but only for  $\tau_{s\perp}$  of Gr-hBN.

The discrepancy of the conventional DP model for  $\tau_{s\parallel}$  of Gr-hBN can be rectified by modifying the model. Briefly, the DP model assumes that  $\mathbf{B}^{\text{in}}$  effectively changes randomly each time the electron scatters. The in-plane magnetic field  $\mathbf{B}_{\parallel}^{\text{in}}$  rotates over the Fermi circle and covers all in-plane directions, satisfying this condition, in both Gr+ $E_{\perp}$  and Gr-hBN. However, the out-of-plane magnetic field  $\mathbf{B}_{\perp}^{\text{in}}$ , which matters only for  $\tau_{s\parallel}$  and is present only for Gr-hBN, has the same direction within each valley. Consequently, only intervalley scattering will change the  $\mathbf{B}_{\perp}^{\text{in}}$  for a given electron spin. As proposed in Ref. 100, this can be captured by changing the DP model from  $(\tau_{s,x}^{\text{DP}})^{-1} \sim \tau_p (\Delta\Omega_{\perp x})^2 = \tau_p \langle \Omega_y^2 + \Omega_z^2 \rangle$  as given by Eq. 82 for in-plane  $x$  spins, to

$$(\tau_{s,x}^{\text{mDP}})^{-1} \approx \tau_p \langle \Omega_y^2 \rangle + \tau_p^{\text{Inter}} \langle \Omega_z^2 \rangle, \quad (89)$$

where  $\tau_p^{\text{Inter}}$  is the intervalley scattering time (dotted line in Fig. 8(d)). This modified DP model agrees with FPDM predictions for  $\tau_{s\parallel}$  of Gr-hBN (Fig. 8(a)).

The ratio  $\tau_{s\perp}/\tau_{s\parallel}$  (Fig. 8(c)) is nearly 1/2 for graphene, consistent with the EY relation Eq. 75 and the fact that  $\langle b_{\parallel}^2 \rangle / \langle b_{\perp}^2 \rangle$  is also 1/2 (Fig. 8(e)). This ratio remains unchanged for Gr+ $E_{\perp}$ , but now because  $(\Delta\Omega_{\perp z})^2 = \langle \Omega_x^2 + \Omega_y^2 \rangle = 2\langle \Omega_y^2 \rangle$ , while  $(\Delta\Omega_{\perp x})^2 = \langle \Omega_y^2 \rangle$  since  $\Omega_z = 0$  (Fig. 8(f)), leading to  $\tau_{s,x}^{\text{DP}} = 2\tau_{s,z}^{\text{DP}}$  using Eq. 82. This ratio deviates substantially from 1/2 only for Gr-hBN (Fig. 8(c)) due to the substrate-induced  $\Omega_z \neq 0$ . The conventional DP model (Eq. 82) only captures part of this dramatic effect seen in the FPDM calculations, while the modifications in Eq. 89 account for  $\Omega_z$  correctly and agree with the FPDM results in Fig. 8(c).



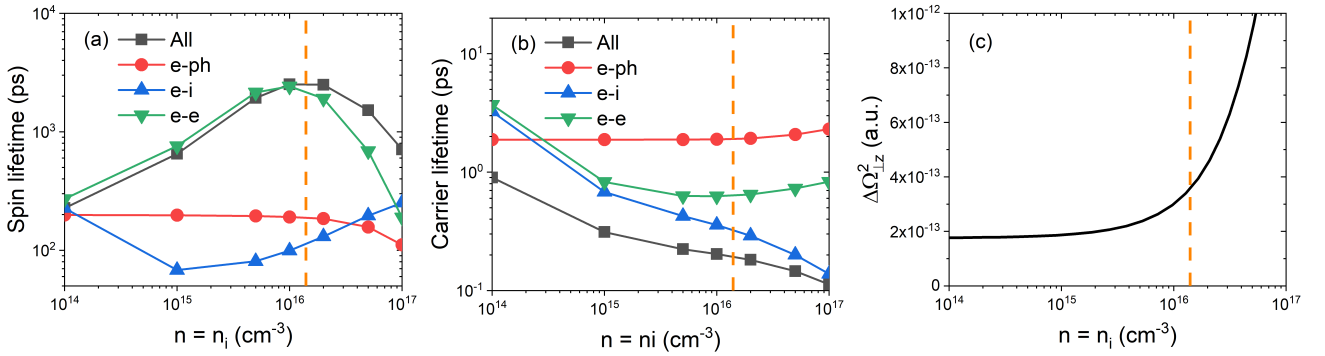


FIG. 7. (a)  $\tau_s$  and (b)  $\tau_p$  of  $n$ -GaAs with different doping concentrations  $n_i$  at 30 K with different scattering mechanisms. “All” represents all the e-ph, e-i and e-e scattering mechanisms being considered. (c)  $\Delta\Omega_{\perp}^2$  as a function of carrier density  $n$ , where  $\Delta\Omega_{\perp}$  is the fluctuation amplitude of Larmor frequency defined in Eq. 81 [16].

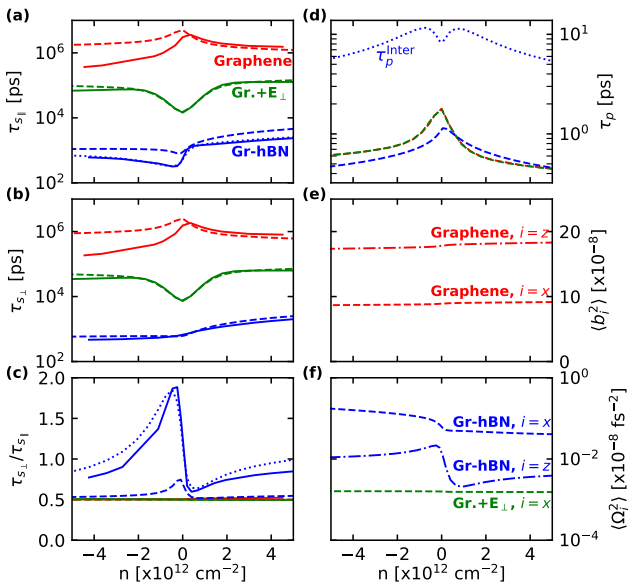


FIG. 8. Theoretical spin and carrier relaxation in graphene (red lines), graphene at  $E_{\perp}=0.4$  V/nm (Gr+ $E_{\perp}$ , green lines) and graphene on hBN (Gr-hBN, blue lines) as a function of  $n$  (positive or negative for electron and hole doping respectively) at room temperature. (a) In-plane spin lifetime  $\tau_{s\parallel}$ , (b) out-of-plane spin lifetime  $\tau_{s\perp}$  and (c) their ratios  $\tau_{s\perp}/\tau_{s\parallel}$  calculated using FPDM approach (solid lines) compared with those estimated from EY/DP models with first-principles inputs (dashed for conventional DP and dotted for modified DP with intervalley scattering contribution lines). (d) Total  $\tau_p$  (three dashed lines) and intervalley only contribution for Gr-hBN (dotted blue line), (e)  $\langle b_i^2 \rangle$  and (f)  $\langle \Omega_i^2 \rangle$ , all predicted from first-principles for the DP and EY models estimates of  $\tau_s$  in (a-c) [20].

$\tau_s$  decrease with increasing carrier density magnitude in graphene (Fig. 8(a,b)), but this trend reverses for both inversion-symmetry-broken cases, in agreement with some experiments.[94, 101] The overall  $\tau_s$  are reduced by one-two orders of magnitude in free-standing

graphene by  $E_{\perp}$  of 0.4 V/nm, down from  $\mu\text{s}$  to tens of ns.  $\langle \Omega_i^2 \rangle$  of Gr-hBN in Fig. 8(f) is about 100 times larger than that of Gr+ $E_{\perp}$ , further reducing  $\tau_s$  of Gr-hBN to the ns scale, comparable to experimental measurements.[94, 96, 97, 102]

Finally,  $\tau_s$  is mostly symmetric between electrons and holes for Gr+ $E_{\perp}$  (Fig. 8(a, b)). However, we find hole  $\tau_s$  to be typically 2-3 times smaller than electrons for both free-standing graphene and Gr-hBN. On hBN, this asymmetry is captured by the (modified) DP model and stems primarily from the larger spin-splitting and hence  $\langle \Omega_i^2 \rangle$  in the valence band compared to the conduction band (not shown), consistent with previous calculations.[103] Importantly, this effect depends sensitively on the substrate, and even on hBN, could reverse for a different layer stacking.[103] Consequently, experiments may find electron-hole asymmetries of either sign depending on the substrate and precise structure,[94, 96–98, 101–103] and we focus here on the comparison between FPDM predictions and DP model for the specific lowest-energy stacking of Gr-hBN.

#### D. Spin dephasing under magnetic field

As introduced in Sec. II B 1, the dephasing time (or transverse time) of a spin ensemble is called  $T_2^*$  and describes the decay of the total excess spin  $\mathbf{S} - \mathbf{S}^{\text{eq}}$  at a nonzero  $\mathbf{B}^{\text{ext}}$  perpendicular to  $\mathbf{S} - \mathbf{S}^{\text{eq}}$ . As discussed in Sec. II A 2,  $T_2^*$  can be simulated straightforwardly through FPDM simulations with Zeeman Hamiltonian considering both spin and orbital angular momenta (Eq. 13 and 14). For the purpose of analysing and understanding spin dephasing, one key parameter is the Landé  $g$ -factor  $\tilde{g}$  (Eq. 86). It value relates to  $\mathbf{B}^{\text{ext}}$ -induced energy splitting (Zeeman effect)  $\Delta E(\mathbf{B}^{\text{ext}})$  and Larmor precession frequency  $\Omega$ , satisfying  $\Omega \approx \Delta E = \mu_B B^{\text{ext}} \tilde{g}$ . More importantly, the  $g$ -factor fluctuation (near Fermi surface or  $\mu_{F,c}$ )  $\Delta\tilde{g}$  (Eq. 87) leads to a nonzero  $\Delta\Omega$  (Eq. 88) and then  $T_2^*$  due to DP or FID mechanism.

Spintronics in halide perovskites has drawn significant

attention in recent years, due to highly tunable spin-orbit fields and intriguing interplay with lattice symmetry. Recently, we simulate[18]  $\tilde{g}$ ,  $\Delta\tilde{g}$  and  $T_2^*$  of a typical halide perovskite - CsPbBr<sub>3</sub>. We find that  $T_2^*$  is sensitive to  $B^{\text{ext}}$  at  $T < 20$  K but not at  $T \geq 20$  K. At 4 K, we predict that  $(T_2^*)^{-1}$  is linear to  $B^{\text{ext}}$  at  $B^{\text{ext}} \geq 0.4$  Tesla and the predicted slope of  $(T_2^*)^{-1}$  is in good agreement with experimental data. Moreover, we predict strong  $n$ -dependence of  $\tilde{g}$ ,  $\Delta\tilde{g}$  and  $T_2^*$ . Together with FPDM simulations of spin relaxation time  $T_1$  of CsPbBr<sub>3</sub> at various conditions, our work provides fundamental insights on how to control and manipulate spin relaxation/dephasing in halide perovskites, which are vital for their spintronics and quantum information applications.

## V. OUTLOOKS

The first-principles density-matrix dynamics (FPDM) approach is an important technique for studying spin and electron dynamics and transport, with outstanding advantages: i) it can accurately describe various interactions, scattering processes, and spin precession simultaneously; ii) it can describe processes far from equilibrium; iii) it can simulate dynamical processes on various time scales from femtoseconds to milliseconds. We have shown its success in simulating ultrafast spin dynamics, spin and charge transport, relaxation and dephasing. In the future study, the FPDM approach still has a broad open area for new theory development.

### 1. Exciton dynamics

Exciton is a bound electron-hole pair generated by optical excitation. Excitons play an important role in optical properties of semiconductors, in particular in low-dimensional systems. Exciton dynamics has been extensively studied using different methods, in particular non-equilibrium Greens' function theory (NEGF) within Kadanoff-Baym equations[45, 104, 105]. We focus on theoretical simulations of exciton spin relaxation based on Lindbladian DM master equation with quantum description of the exciton-phonon scattering. Understanding the exciton spin relaxation is also important for understanding optical measurements of spin dynamics. By replacing electrons to excitons, the existing FPDM approach can be generalized to simulation spin dynamics of excitons. The exciton dynamics can involve many types of processes including exciton-light interaction, exciton-phonon scattering, phonon-mediated exciton recombination and dissociation, exciton-exciton annihilation, etc. Initially, we will focus on exciton-light interaction and exciton-phonon scattering, which are two most important processes leading to exciton spin relaxation.

The exciton-light interaction is responsible to exciton spin generation by light absorption with a circularly-polarized pump pulse and exciton spin relaxation

through exciton-phonon scattering and exciton radiative recombination. The light absorption for excitons is similar to that for electrons (see Sec. II A 2) except that the momentum matrix elements are now between two excitonic states [106–108].

The exciton-phonon scattering is responsible to exciton spin relaxation. According to Refs. 109, 110, the exciton-phonon scattering matrix elements can be approximately obtained from the excitation wavefunction at finite momentum and electron-phonon scattering matrix elements. Recently we implemented the exciton-phonon scattering matrix elements and used them to simulate phonon-assisted indirect exciton radiative recombination. In the density-matrix master equation, the term of the exciton-phonon scattering is rather similar to the electron-phonon scattering, except that the excitons are bosons while the electrons are fermions. Therefore, the implementation of the exciton-phonon scattering in the frame of FPDM approach can be straightforward.

### 2. Circular photogalvanic effect (CPGE)

CPGE is the effect that under the circularly-polarized light a DC current may be induced in a solid-state material, and widely presents in materials without inversion symmetry, in absence of p-n junction and applied electric field. In recent years, CPGE has attracted growing interests in the fields of topological physics and spinoptotronics [111, 112]. In order to deeply understand CPGE, theoretical methods have been developed based on perturbation theory. However, several critical issues remain: (i) the scattering mechanisms are highly simplified with a single relaxation time approximation; (ii) spontaneous recombination was rarely considered; (iii) available theory requires different formulation for each contribution i.e. interband or intraband contributions; (iv) many-body effects were not considered. These issues may be resolved based on our FPDM approach.

If a constant laser field is applied to an inversion symmetry broken system, the quantum master equation for describing density matrix of the electronic system reads:

$$\frac{d\rho}{dt} = \frac{d\rho}{dt}|_{\text{laser}} + \frac{d\rho}{dt}|_{\text{sp-em}} + \frac{d\rho}{dt}|_{\text{e-ph}}, \quad (90)$$

where  $\frac{d\rho}{dt}|_{\text{laser}}$  is coherent dynamics due to a laser field (Eq. 12),  $\frac{d\rho}{dt}|_{\text{sp-em}}$  and  $\frac{d\rho}{dt}|_{\text{e-ph}}$  are the spontaneous emission (Eq. 36) and e-ph scattering terms (Eq. 17 and 18), respectively.

CPGE is measuring the steady state current when a nonmagnetic system is under a constant circularly-polarized laser field for a long enough time. In the velocity gauge, the current density is computed using[32]

$$\mathbf{J} = \text{Tr}(\rho \mathbf{j}), \quad (91)$$

$$\mathbf{j}_{kmn}(t) = -e \left( \mathbf{v}_{kmn} + \delta_{mn} \frac{e}{m_e} \mathbf{A}(t) \right), \quad (92)$$

where  $\mathbf{v}$  is the velocity operator matrix and  $\mathbf{v} = \mathbf{p}/m_e$ . The average value of the second term of  $\mathbf{j}$  is usually zero so that this term does not contribute to CPGE.

### 3. More on scattering terms

Although in our FPDM approach, the *ab-initio* treatment of quantum scattering is rather general, the following theoretical development can further improve the applicability of our methods to different systems:

*Anharmonic phonons.* In current implementation, phonons are harmonic and it is required that the material must be dynamically stable at zero temperature. However, for some soft materials (e.g., hybrid halide perovskites), significant anharmonic effects appear at high- $T$  phase, which requires extracting phonon properties from finite-temperature simulations, e.g. using *ab-initio* molecular dynamics. Such approach has been implemented [113] for studying phonon, electron-phonon, and carrier transport properties, which can be also applied to study the anharmonic effect on spin relaxation under our FPDM framework.

*Fröhlich interaction and LO-TO splitting in doped semiconductor.* The intraband dielectric screening is not considered for Fröhlich interaction and LO-TO splitting in current implementation. This may be problematic in doped semiconductor and may lead to significant errors at moderate or high carrier density.

Since we have already implemented the intraband dielectric function (Eq. 33), its effect can be straightforwardly included in FPDM approach similar to Ref. 114.

*Short-range contribution to the electron-ionized-impurity scattering.* For the electron-ionized-impurity scattering, we currently only consider the long-range contribution. This is appropriate for certain systems like GaAs, but may be problematic when intravalley processes dominate spin relaxation or the short-range spin-flip electron-ionized-impurity scattering is unimportant to spin relaxation. Therefore, it is important to include both long-range and short-range contributions to the electron-ionized-impurity scattering. Similar to Ref. 56, the long-range and short-range parts are treated separately - the short-range part is treated from first principles similar to neutral impurity, and the long-range part is simulated using the screened Coulomb potential.

### ACKNOWLEDGEMENTS

This work is supported by National Science Foundation under grant No. DMR-1956015. This research used resources of the Center for Functional Nanomaterials, which is a US DOE Office of Science Facility, and the Scientific Data and Computing center, a component of the Computational Science Initiative, at Brookhaven National Laboratory under Contract No. DE-SC0012704, the lux supercomputer at UC Santa Cruz, funded by NSF MRI grant AST 1828315, the National Energy Research Scientific Computing Center (NERSC) a U.S. Department of Energy Office of Science User Facility operated under Contract No. DE-AC02-05CH11231, the Extreme Science and Engineering Discovery Environment (XSEDE) which is supported by National Science Foundation Grant No. ACI-1548562 [115].

- 
- [1] A. Avsar, H. Ochoa, F. Guinea, B. Özyilmaz, B. J. van Wees, and I. J. Vera-Marun, *Rev. Mod. Phys.* **92**, 021003 (2020).
  - [2] J. F. Sierra, J. Fabian, R. K. Kawakami, S. Roche, and S. O. Valenzuela, *Nat. Nanotechnol* **16**, 856 (2021).
  - [3] J. H. Garcia, M. Vila, C.-H. Hsu, X. Waintal, V. M. Pereira, and S. Roche, *Phys. Rev. Lett.* **125**, 256603 (2020).
  - [4] L. Šmejkal, Y. Mokrousov, B. Yan, and A. H. MacDonald, *Nat. Phys.* **14**, 242 (2018).
  - [5] Y.-H. Kim, Y. Zhai, H. Lu, X. Pan, C. Xiao, E. A. Gaulding, S. P. Harvey, J. J. Berry, Z. V. Vardeny, J. M. Luther, *et al.*, *Science* **371**, 1129 (2021).
  - [6] L. Zhang, J. Jiang, C. Multunas, C. Ming, Z. Chen, Y. Hu, Z. Lu, S. Pendse, R. Jia, M. Chandra, *et al.*, *Nat. Photon.*, 1 (2022).
  - [7] I. Žutić, J. Fabian, and S. D. Sarma, *Rev. Mod. Phys.* **76**, 323 (2004).
  - [8] M. Wu, J. Jiang, and M. Weng, *Phys. Rep.* **493**, 61 (2010).
  - [9] O. D. Restrepo and W. Windl, *Phys. Rev. Lett.* **109**, 166604 (2012).
  - [10] D. V. Fedorov, M. Gradhand, S. Ostanin, I. V. Maznichenko, A. Ernst, J. Fabian, and I. Mertig, *Phys. Rev. Lett.* **110**, 156602 (2013).
  - [11] M. A. L. Marques, N. T. Maitra, F. M. S. Nogueira, E. K. U. Gross, and A. Rubio, *Fundamentals of Time-Dependent Density Functional Theory*, Vol. 837 (Springer Science & Business Media, 2012).
  - [12] Z. Chen and L. Wang, *Sci. Adv.* **5**, eaau8000 (2019).
  - [13] S. R. Acharya, V. Turkowski, G. P. Zhang, and T. S. Rahman, *Phys. Rev. Lett.* **125**, 017202 (2020).
  - [14] K. Krieger, J. K. Dewhurst, P. Elliott, S. Sharma, and E. K. U. Gross, *J. Chem. Theory Comput.* **11**, 4870 (2015).
  - [15] J. Park, J.-J. Zhou, Y. Luo, and M. Bernardi, *Phys. Rev. Lett.* **129**, 197201 (2022).

- [16] J. Xu, A. Habib, R. Sundararaman, and Y. Ping, *Phys. Rev. B* **104**, 184418 (2021).
- [17] J. Xu, A. Habib, S. Kumar, F. Wu, R. Sundararaman, and Y. Ping, *Nat. Commun.* **11**, 2780 (2020).
- [18] J. Xu, K. Li, U. N. Huynh, J. Huang, R. Sundararaman, V. Vardeny, and Y. Ping, Preprint at <https://arxiv.org/abs/2210.17074> (2023).
- [19] J. Xu, H. Takenaka, A. Habib, R. Sundararaman, and Y. Ping, *Nano Lett.* **21**, 9594 (2021).
- [20] A. Habib, J. Xu, Y. Ping, and R. Sundararaman, *Phys. Rev. B* **105**, 115122 (2022).
- [21] J. Xu and Y. Ping, *npj Comput. Mater.* **9**, 47 (2023).
- [22] F. Rossi and T. Kuhn, *Rev. Mod. Phys.* **74**, 895 (2002).
- [23] M. Bonitz, *Quantum Kinetic Theory* (Springer, Cham, 2016).
- [24] V. M. Axt and A. Stahl, *Z. Physik B - Condensed Matter* **93**, 195 (1994).
- [25] R. C. Iotti and F. Rossi, *Eur. Phys. J. B* **90**, 1 (2017).
- [26] A. Marini, in *Journal of Physics: Conference Series*, Vol. 427 (IOP Publishing, 2013) p. 012003.
- [27] W. Kohn and J. Luttinger, *Phys. Rev.* **108**, 590 (1957).
- [28] J. Krieger and G. Iafrate, *Phys. Rev. B* **35**, 9644 (1987).
- [29] E. Ciancio, R. C. Iotti, and F. Rossi, *Phys. Rev. B* **69**, 165319 (2004).
- [30] G. Kané, M. Lazzari, and F. Mauri, *Phys. Rev. B* **86**, 155433 (2012).
- [31] A. Sekine, D. Culcer, and A. H. MacDonald, *Phys. Rev. B* **96**, 235134 (2017).
- [32] G. Ventura, D. Passos, J. L. Dos Santos, J. V. P. Lopes, and N. Peres, *Phys. Rev. B* **96**, 035431 (2017).
- [33] G. Iafrate, V. Sokolov, and J. Krieger, *Phys. Rev. B* **96**, 144303 (2017).
- [34] R. D. King-Smith and D. Vanderbilt, *Phys. Rev. B* **47**, 1651 (1993).
- [35] R. Resta, *Rev. Mod. Phys.* **66**, 899 (1994).
- [36] C. Multunas, A. Grieder, J. Xu, Y. Ping, and S. R., Under Preparation (2022).
- [37] R. Rosati, R. C. Iotti, F. Dolcini, and F. Rossi, *Phys. Rev. B* **90**, 125140 (2014).
- [38] F. Giustino, *Rev. Mod. Phys.* **89**, 015003 (2017).
- [39] R. Sundararaman and Y. Ping, *J. Chem. Phys.* **146**, 104109 (2017).
- [40] C. Jacoboni, *Theory of Electron Transport in Semiconductors: A Pathway from Elementary Physics to Nonequilibrium Green Functions*, Vol. 165 (Springer Science & Business Media, 2010).
- [41] X. Wu, D. Vanderbilt, and D. R. Hamann, *Phys. Rev. B* **72**, 035105 (2005).
- [42] C. Lü, J. Cheng, M. Wu, and I. da Cunha Lima, *Phys. Lett. A* **365**, 501 (2007).
- [43] F. Meier and B. P. Zakharchenya, *Optical Orientation* (Elsevier, 2012).
- [44] M. P. M. Dean, Y. Cao, X. Liu, S. Wall, D. Zhu, R. Mankowsky, V. Thampy, X. M. Chen, J. G. Vale, D. Casa, *et al.*, *Nat. Mater.* **15**, 601 (2016).
- [45] A. Molina-Sánchez, D. Sangalli, L. Wirtz, and A. Marini, *Nano Lett.* **17**, 4549 (2017).
- [46] N. Mainkar, D. A. Browne, and J. Callaway, *Phys. Rev. B* **53**, 3692 (1996).
- [47] J. M. Kikkawa and D. D. Awschalom, *Phys. Rev. Lett.* **80**, 4313 (1998).
- [48] A. V. Kimel, F. Bentivegna, V. N. Gridnev, V. V. Pavlov, R. V. Pisarev, and T. h. Rasing, *Phys. Rev. B* **63**, 235201 (2001).
- [49] R. Sundararaman, K. Letchworth-Weaver, K. A. Schwarz, D. Gunceler, Y. Ozhabes, and T. A. Arias, *SoftwareX* **6**, 278 (2017).
- [50] N. Marzari and D. Vanderbilt, *Phys. Rev. B* **56**, 12847 (1997).
- [51] A. M. Brown, R. Sundararaman, P. Narang, W. A. Goddard, and H. A. Atwater, *ACS Nano* **10**, 957 (2016).
- [52] P. Narang, L. Zhao, S. Claybrook, and R. Sundararaman, *Adv. Opt. Mater.* **5**, 1600914 (2017).
- [53] A. M. Brown, R. Sundararaman, P. Narang, A. M. Schwartzberg, W. A. Goddard III, and H. A. Atwater, *Phys. Rev. Lett.* **118**, 087401 (2017).
- [54] A. Habib, R. Florio, and R. Sundararaman, *J. Opt.* **20**, 064001 (2018).
- [55] A. M. Brown, R. Sundararaman, P. Narang, W. A. Goddard III, and H. A. Atwater, *Phys. Rev. B* **94**, 075120 (2016).
- [56] C. Verdi and F. Giustino, *Phys. Rev. Lett.* **115**, 176401 (2015).
- [57] T. Sohler, M. Gibertini, M. Calandra, F. Mauri, and N. Marzari, *Nano Lett.* **17**, 3758 (2017).
- [58] R. C. Iotti and F. Rossi, *Phys. Rev. Lett.* **87**, 146603 (2001).
- [59] H. Watanabe and Y. Yanase, *Phys. Rev. X* **11**, 011001 (2021).
- [60] R. Kubo, *Rep. Prog. Phys.* **29**, 255 (1966).
- [61] T. Maassen, F. Dejene, M. Guimarães, C. Józsa, and B. Van Wees, *Physical Review B* **83**, 115410 (2011).
- [62] C. J. Ciccarino, T. Christensen, R. Sundararaman, and P. Narang, *Nano Lett.* **18**, 5709 (2018).
- [63] T. Gunst, T. Markussen, K. Stokbro, and M. Brandbyge, *Phys. Rev. B* **93**, 035414 (2016).
- [64] G. D. Mahan, *Many-Particle Physics* (Springer US, 2000).
- [65] J. Fabian and S. D. Sarma, *Phys. Rev. Lett.* **81**, 5624 (1998).
- [66] W. Leyland, R. Harley, M. Henini, A. Shields, I. Farrer, and D. Ritchie, *Phys. Rev. B* **76**, 195305 (2007).
- [67] Y. Yafet, in *Solid state physics*, Vol. 14 (Elsevier, 1963) pp. 1–98.
- [68] Z. Yu, *Sci. Rep.* **6**, 1 (2016).
- [69] E. Kirstein, D. Yakovlev, M. Glazov, E. Zhukov, D. Kudlacik, I. Kalitukha, V. Sapega, G. Dimitriev, M. Semina, M. Nestoklon, *et al.*, *Nat. Commun.* **13**, 1 (2022).
- [70] D. J. Lepine, *Phys. Rev. B* **6**, 436 (1972).
- [71] B. Huang, D. J. Monsma, and I. Appelbaum, *Phys. Rev. Lett.* **99**, 177209 (2007).
- [72] P. Dey, L. Yang, C. Robert, G. Wang, B. Urbaszek, X. Marie, and S. A. Crooker, *Phys. Rev. Lett.* **119**, 137401 (2017).
- [73] J. Li, M. Goryca, K. Yumigeta, H. Li, S. Tongay, and S. A. Crooker, *Phys. Rev. Mater.* **5**, 044001 (2021).
- [74] M. Goryca, N. P. Wilson, P. Dey, X. Xu, and S. A. Crooker, *Sci. Adv.* **5**, eaau4899 (2019).
- [75] X. Song, S. Xie, K. Kang, J. Park, and V. Sih, *Nano Lett.* **16**, 5010 (2016).
- [76] T. Yan, S. Yang, D. Li, and X. Cui, *Phys. Rev. B* **95**, 241406 (2017).
- [77] D. Edelberg, D. Rhodes, A. Kerelsky, B. Kim, J. Wang, A. Zangiabadi, C. Kim, A. Abhinandan, J. Ardelean, M. Scully, *et al.*, *Nano Lett.* **19**, 4371 (2019).
- [78] D. Rhodes, S. H. Chae, R. Ribeiro P., and J. Hone, *Nat. Mater.* **18**, 541 (2019).

- [79] M. Yankowitz, D. McKenzie, and B. J. LeRoy, *Phys. Rev. Lett.* **115**, 136803 (2015).
- [80] D. Van Tuan, F. Ortmann, A. W. Cummings, D. Soriano, and S. Roche, *Sci. Rep.* **6**, 1 (2016).
- [81] C. Ertler, S. Kunschuh, M. Gmitra, and J. Fabian, *Phys. Rev. B* **80**, 041405 (2009).
- [82] L. Tao and E. Y. Tsybal, *Phys. Rev. B* **100**, 161110 (2019).
- [83] D. J. Hilton and C. L. Tang, *Phys. Rev. Lett.* **89**, 146601 (2002).
- [84] J. H. Jiang and M. W. Wu, *Phys. Rev. B* **79**, 125206 (2009).
- [85] A. Kamra and B. Ghosh, *J. Appl. Phys* **109**, 024501 (2011).
- [86] F. Dettwiler, J. Fu, S. Mack, P. J. Weigele, J. C. Egues, D. D. Awschalom, and D. M. Zumbühl, *Phys. Rev. X* **7**, 031010 (2017).
- [87] D. Huber, M. Reindl, S. F. C. Da Silva, C. Schimpf, J. Martín-Sánchez, H. Huang, G. Piredda, J. Edlinger, A. Rastelli, and R. Trotta, *Phys. Rev. Lett.* **121**, 033902 (2018).
- [88] V. V. Belykh, A. Y. Kuntsevich, M. M. Glazov, K. V. Kavokin, D. R. Yakovlev, and M. Bayer, *Phys. Rev. X* **8**, 031021 (2018).
- [89] Y. Ohno, R. Terauchi, T. Adachi, F. Matsukura, and H. Ohno, *Phys. Rev. Lett.* **83**, 4196 (1999).
- [90] P. E. Hohage, G. Bacher, D. Reuter, and A. D. Wieck, *Appl. Phys. Lett.* **89**, 231101 (2006).
- [91] Z. G. Yu, S. Krishnamurthy, M. Van Schilfgaarde, and N. Newman, *Phys. Rev. B* **71**, 245312 (2005).
- [92] M. D. Mower, G. Vignale, and I. V. Tokatly, *Phys. Rev. B* **83**, 155205 (2011).
- [93] G. Marchetti, M. Hodgson, J. McHugh, R. Chantrell, and I. D'Amico, *Materials* **7**, 2795 (2014).
- [94] M. Drogeler, C. Franzen, F. Volmer, T. Pohlmann, L. Banszerus, M. Wolter, K. Watanabe, T. Taniguchi, C. Stampfer, and B. Beschoten, *Nano Lett.* **16**, 3533 (2016).
- [95] C. R. Dean, A. F. Young, I. Meric, C. Lee, L. Wang, S. Sorgenfrei, K. Watanabe, T. Taniguchi, P. Kim, K. L. Shepard, and J. Hone, *Nat. Nanotechnol.* **5**, 722 (2010).
- [96] W. Han and R. K. Kawakami, *Phys. Rev. Lett.* **107**, 047207 (2011).
- [97] M. H. Guimarães, P. J. Zomer, J. Ingla-Aynés, J. C. Brant, N. Tombros, and B. J. van Wees, *Phys. Rev. Lett.* **113**, 086602 (2014).
- [98] B. Raes, J. E. Scheerder, M. V. Costache, F. Bonell, J. F. Sierra, J. Cuppens, J. Van de Vondel, and S. O. Valenzuela, *Nat. Commun.* **7**, 11444 (2016).
- [99] M. H. Guimarães, A. Veligura, P. Zomer, T. Maassen, I. Vera-Marun, N. Tombros, and B. Van Wees, *Nano Letters* **12**, 3512 (2012).
- [100] A. W. Cummings, J. H. Garcia, J. Fabian, and S. Roche, *Phys. Rev. Lett.* **119**, 206601 (2017).
- [101] P. J. Zomer, M. H. D. Guimarães, N. Tombros, and B. J. van Wees, *Phys. Rev. B* **86**, 161416(R) (2012).
- [102] M. V. Kamalakar, C. Groenveld, A. Dankert, and S. P. Dash, *Nat. Commun.* **6**, 1 (2015).
- [103] K. Zollner, M. Gmitra, and J. Fabian, *Phys. Rev. B* **99**, 125151 (2019).
- [104] F. Paleari and A. Marini, *Physical Review B* **106**, 125403 (2022).
- [105] Y.-H. Chan, D. Y. Qiu, F. H. da Jornada, and S. G. Louie, *Proceedings of the National Academy of Sciences* **118**, e1906938118 (2021).
- [106] C. Guo, J. Xu, and Y. Ping, *Journal of Physics: Condensed Matter* **33**, 234001 (2021).
- [107] F. Wu, D. Rocca, and Y. Ping, *J. Mater. Chem. C* **7**, 12891 (2019).
- [108] T. J. Smart, K. Li, J. Xu, and Y. Ping, *npj Computational Materials* (2021).
- [109] G. Antonius and S. G. Louie, *Phys. Rev. B* **105**, 085111 (2022).
- [110] H.-Y. Chen, D. Sangalli, and M. Bernardi, *Physical Review Letters* **125**, 107401 (2020).
- [111] H. Watanabe and Y. Yanase, *Phys. Rev. X* **11**, 011001 (2021).
- [112] F. de Juan, A. G. Grushin, T. Morimoto, and J. E. Moore, *Nat. Commun.* **8**, 15995 (2017).
- [113] O. Hellman, P. Steneteg, I. A. Abrikosov, and S. I. Simak, *Physical Review B* **87**, 104111 (2013).
- [114] F. Macheda, P. Barone, and F. Mauri, *Physical Review Letters* **129**, 185902 (2022).
- [115] J. Towns, T. Cockerill, M. Dahan, I. Foster, K. Gauthier, A. Grimshaw, V. Hazlewood, S. Lathrop, D. Lifka, G. D. Peterson, R. Roskies, J. R. Scott, and N. Wilkins-Diehr, *Comput. Sci. Eng.* **16**, 62 (2014).